Critical Review of Recent Advancement in Metamaterial Design for Wireless Power Transfer

WEBSTER ADEPOJU[1], (Student Member, IEEE),
INDRANIL BHATTACHARYA[1], (Member, IEEE), **MARY SANYAOLU**[2],
MUHAMMAD ENAGI BIMA[3], (Student Member, IEEE), **TRAPA BANIK**[1],
EBRAHIM N. ESFAHANI[1], **AND OLATUNJI ABIODUN**[1]

[1]Department of Electrical and Computer Engineering, Tennessee Technological University, Cookeville, TN 38505, USA
[2]GasFleet Engineering, Lagos 100267, Nigeria
[3]Norstrum Inc., Atlanta, GA 30326, USA

Corresponding authors: Webster Adepoju (woadepoju42@tntech.edu) and Indranil Bhattacharya (ibhattacharya@tntech.edu)

ABSTRACT With increasing penetration of wireless charging technologies comes an ever-rising demand for wireless power transfer (WPT) structures that demonstrate high power transfer and power transfer efficiency (PTE), especially over wide transfer distance. The concern with reliability in adopting wireless charging technologies in consumer and industrial applications (including mobile chargers and dynamic wireless charging of electric vehicles, EVs) stems from fluctuating output power and low power transfer efficiency (PTE). Moreover, the inherently high resonant frequency of existing metamaterial (MM)-based WPT designs imposes a high switching stress on power semiconductors and passive components, resulting in high power dissipation, especially in high power applications. This manuscript presents a critical survey of recent studies and developments in MM-based WPT systems. First, the fundamental concepts and classification of WPT technologies based on magnetic resonant coupling (MRC), inductive coupling etc. are discussed. Going forward, key MM design considerations, including resonance operating frequencies, effective permittivity (ϵ_r), effective permeability (μ_r), numerical modeling, equivalent circuit representations, and 3D fabrication technologies are widely analyzed and critiqued. Additionally, the performance enhancing effect of integrating different MM designs with existing WPT systems are explicitly discussed. Finally, the technical challenges associated with the resonant operating frequencies of MM, miniaturization of MM design footprint, and 3D prototyping are investigated while also presenting potential solutions.

INDEX TERMS Wireless power transfer (WPT), metamaterial (MM), power transfer efficiency (PTE), resonant frequency, transmit power, effective permeability, electric vehicle (EV).

I. INTRODUCTION

Since first discovered by Nikola Tesla in 1914 [1], and subsequently reported by Heinrich Hertz and Oliver Lodge [2], Wireless Power Transfer (WPT) has become a focal point of numerous research interests and an alternative power transmission mechanism in mobile computing [3], [4], wireless charging of biomedical body implants [5]–[7] and Electric Vehicle (EV) [8]. This breakthrough in WPT research can be attributed to improved performance of power electronic components and the discovery of wide band gap power semiconductors, capable of operating at high switching frequencies with minimal losses [4]. As part of the development in wireless charging technology, frantic

The associate editor coordinating the review of this manuscript and approving it for publication was Philip Pong.

research effort has culminated in the exploitation of concept like resonant magnetic resonance coupling (MRC) to transfer $60W$ of power over a transmission distance of 2m [9]. In addition, as recently as 2018, a $120kW$ EV wireless charging prototype was announced by the Oak Ridge National Laboratory (ORNL) as part of the broader plan to extend the reach and range of WPT application [10]. While this prototype is not yet commercialized to fully understand its inherent operational challenges, it is reputed as the state of the art in high power wireless charging applications. Moreover, it is worth noting that despite the progress made in the penetration of wireless technologies, the earlier envisaged spread in its adoption is largely hampered by a diminution in coupling coefficient (κ_c), transfer power and power transfer efficiency (PTE), especially as the distance between the transmitting coil (Tx) and receiving
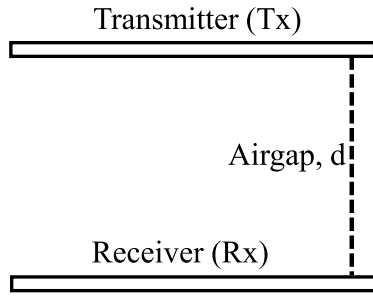
FIGURE 1. Schematic of a two-coil WPT structure, showing the transmitting coil (Tx), and receiving coil (Rx) for wireless power transfer.

FIGURE 2. General classification of wireless power transfer technology.

coil (Rx) increases. In order to address these issues, various WPT concepts, including inductive coupling (IC) [11]–[13] and Magnetic Resonance Coupling (MRC) [9], [14]–[17] have been developed to enhance the performance of WPT; however, their operation is handicapped by a continuous power decay coupled with a reduction in PTE as the transfer distance increases. Further, the mutual coupling, k_c, diminishes by approximately the cube inverse of the coil separation ($\approx 1/d^3$), essentially limiting the applications where efficient WPT can be achieved to those requiring mid-range distances, which is about $\times 4$ the radius of either *Tx* or *Rx*. Besides, the internal parasitic inductance, capacitance and resistance of these coils generate stray, magnetic, capacitive and resistive losses whose cumulative effect significantly reduces the output power and PTE. As showcased in Fig. 1, when the air-gap, d, increases; the magnetic coupling between the *Tx* and *Rx* weakens, effectively forcing the induced magnetic field to travel a longer distance before reaching the receiver. The farther the traveling distance of the magnetic flux, the greater its divergence, leading to flux leakage, increased power loss and reduction in overall PTE of the system. The general relationship connecting the mutual inductance, M_{TxRx}, coupling co-efficient, κ_c and self inductance of the transmitter (L_{TX}) and receiver (L_{RX}) circuits of a WPT system is shown in (1)

$$\kappa_c = \frac{M_{TXRX}}{\sqrt{L_{TX}L_{RX}}} \in \{\leq 0, \leq 1\} \qquad (1)$$

where L_{Tx} and L_{Rx} are the self inductance of *Tx* and *Rx*, respectively, whereas $\kappa_c \leq 0$ and $\kappa_c = 1$ are the coupling factor of two loosely coupled resonators and two strongly coupled resonators, respectively. Essentially, the negative value of mutual coupling ($\kappa_c < 0$) can be explained by the magnetic flux cancellation theory, in which case the magnetic flux generated by *Tx* and *Rx* partly cancels each other in the far away partly overlapped state.

In general, MRC-based WPT can be realized by matching the resonant frequency of both *Tx* and *Rx* [18]. Fig. 2 shows the general classification of a WPT system. Both inductive and MRC-based WPT are categorized as near-field and exploits a conventional two coil [19], three coil [20] and four coil structures [21] for coupling of near magnetic field with the end goal of enhancing the transfer power
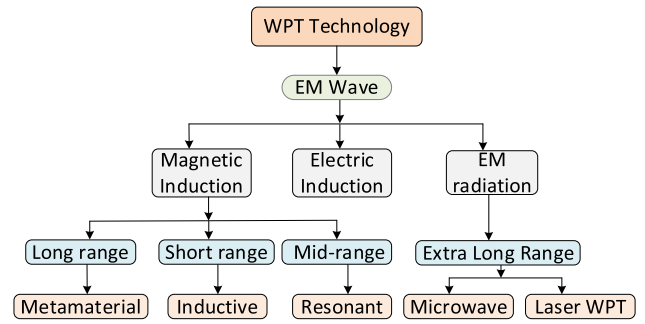
and overall efficiency of the system. For the capacitive and inductive WPT designs introduced by Tesla [5], [22], it was discovered that high power transfer distance and by extension, enhanced coupling efficiency can be achieved by tuning the inductance and capacitance of the transmitter and receiver's compensation network to optimal value, leading to frequency matching and a strong coupling of the resonators. Moreover, microwave and laser-based WPT designs utilize high operating frequency in the order of GigaHertz to transmit power over a very long distance. This is known as far-field or radiative WPT. In other studies, various optimization techniques including adaptive matching techniques [23], frequency matching approach [24], meta-heuristic-based Jaya and crow search algorithms have been adopted to improve the performance of WPT systems [25]. Both Jaya and Crow search algorithm harness a teaching-learning strategy to tune the calculated results towards the desired or optimal goal. While these optimization techniques have shown great effectiveness in enhancing WPT performance, it is notable that the resulting transfer power and PTE based on these optimization techniques pale in comparison to the enormous power demand of existing power electronic components.

The rest of the manuscript is structured as follows: Section II presents a brief description and general background of magnetically coupled resonant WPT systems. Similarly, Section III showcases a concise yet detail description of the evolution of MM-based WPT designs ever since its first discovery. Besides, a general overview of existing MM-designs based on the operating resonant frequencies, design geometries, substrate materials, effective permeability and permittivity is elicited in this section. Further, Section IV describes the underpinning technology and physics of MM-based WPT system In addition, the section presents a categorization of existing MM-WPT based on 1-dimensional (D), 2D, and 3D designs is concisely. Further, an expounded critical literature survey of different positioning of MM-slabs in a WPT system is explicated in section V while section VI describes the numerical model and equivalent circuit representation of MM-based WPT system coupled optimal placement of MM-slab for enhanced PTE and improved WPT performance.
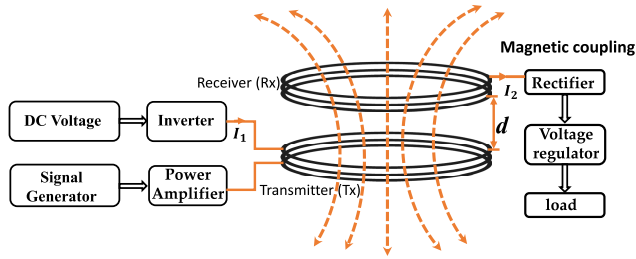
FIGURE 3. Schematic configuration of an MCR-WPT system, comprising resonance coils, an inverter, rectifier and DC-DC converter.
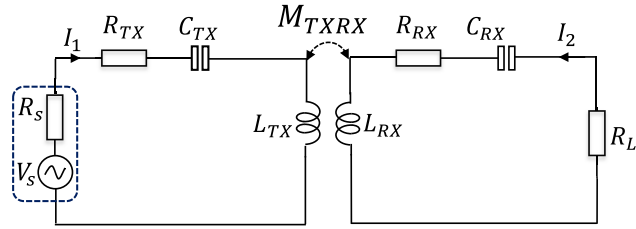

FIGURE 4. Simplified circuit diagram of a two coil WPT structure.

II. WIRELESS POWER TRANSFER BASED ON MAGNETIC RESONANT COUPLING (MCR-WPT)

The typical configuration of an MCR-WPT system consisting of resonance coils and power electronic systems, including inverter, rectifier and DC-DC converter/ voltage regulator is shown in Fig. 3. However, for WPT systems operating in high MHz frequency range, efficient power transfer is not achievable due to the fact that high frequency increases the switching transition of power semiconductor which results in high switching stress, high switching losses and power dissipation. To mitigate the losses, RF power amplifier has been adopted for use in resonant system [15]. The diagrammatic representation of a simplified two coil WPT structure is displayed in Fig. 4. It consists of two resonant coils, a voltage source (V_s, source resistance, R_s, and a load resistance, R_L. Using Kirchoff's Voltage Law (KVL), the analysis of the simplified two coil WPT structure in Fig. 4 expressed in matrix form is shown in (44),

$$\begin{bmatrix} V_s \\ 0 \end{bmatrix} = \begin{bmatrix} R_s + Z_{TX} & jwM_{TXRX} \\ jwM_{TXRX} & Z_{RX} + R_L \end{bmatrix} \begin{bmatrix} I_1 \\ I_2 \end{bmatrix} \quad (2)$$

where

$$Z_{TX} = R_{TX} + j\left[\omega L_{TX} - \frac{1}{\omega C_{TX}}\right] \quad (3)$$

$$Z_{RX} = R_{RX} + j\left[\omega L_{RX} - \frac{1}{\omega C_{RX}}\right] \quad (4)$$

Using the equivalent circuit in Fig. 5 and analyzing in tandem with [26], the reflected impedance, Z_r from the receiver to the transmitter coil based on is derived as

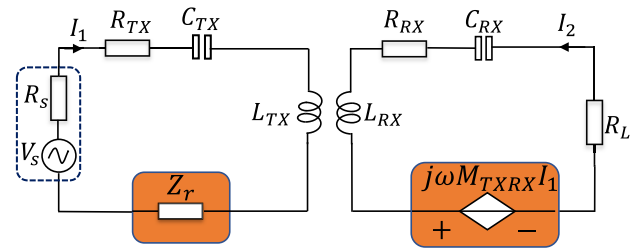$$Z_r = \frac{[\omega M_{TXRX}]^2}{R_L + j\left[\omega L_{RX} - \frac{1}{\omega C_{RX}}\right]} \quad (5)$$

FIGURE 5. Equivalent circuit depiction of Fig. 4 showing -LEFT- the reflection of receiver (*Rx*) on transmitter (*Tx*)- Right- the reflection of *Tx* on *Rx*.

The corresponding output power at the load resistance and PTE of the system are derived as shown in (6) and (7), respectively.

$$P_{out} = \frac{(\omega k_c V_s)^2 L_{TX} L_{RX}}{(R_L + R_{RX})((R_s + R_{TX})^2 + (\omega k_c)^2 L_{TX} L_{RX})} \quad (6)$$

$$\eta = \frac{\omega^2 k_c^2 L_{TX} L_{RX}}{(R_L + R_{RX})(R_s + R_{TX}) + \omega^2 k_c^2 L_{TX} L_{RX}} \quad (7)$$

where ω is the operating frequency expressed as $\omega = 2\pi f_r$ and f_r is the resonance frequency of the coils. Alternatively, the PTE can be expressed as a function of the reflected impedance and the resistance at resonance as seen in (8)

$$\eta = \frac{Z_r}{Z_r + R_s + R_{TX}} \times \frac{R_L}{R_L + R_{RX}} \quad (8)$$

Assuming the magnetic coupling between the two coils is known, the optimal load, $R_{L(opt)}$, corresponding to maximum efficiency, η_{max}, can be obtained by taking a partial differential of (7) with respect to R_L ($\frac{\partial \eta}{\partial R_L} = 0$) as seen in (9)

$$R_{L(opt)} = \sqrt{\frac{R_{RX}}{R_{TX}}\left((\omega_s M_{TXRX})^2 + (R_{RX})^2\right)} \quad (9)$$

III. OVERVIEW OF METAMATERIAL (MM) BASED WPT SYSTEM

In recent times, MM has become an attractive option for improving the performance of WPT systems, especially, for transfer distance in excess of ×4 the diameter of exciting coils [13], [27], [28]. This is fueling its increasing adoption in satellite technologies [29]–[31], biomedical implants [32]–[35] as exemplified in the wireless charging of cardiac pacemakers coupled with RF and microwave applications [36]–[39]. The presence of evanescent wave and magneto-inductive waves in a MM structure accounts for the amplification of magnetic field in a wave propagating media, effectively improving the overall performance of a WPT system. It is worth stating that the enhancement ability of MMs stems from the alteration in their physical structures coupled with their flexibility to be embedded with highly conductive artificial inclusions, leading to the creation of efficient homogeneous media. The schematic in Fig. 6
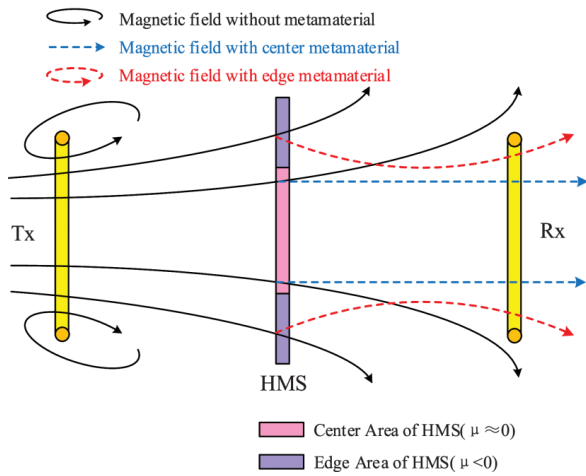
FIGURE 6. Impact of hybrid meta-material (HMS) structure on magnetic field distribution in a WPT system.

FIGURE 7. Classification of metamaterial (MM) Based on the polarity of effective permeability, (μ_r) and effective permittivity (ϵ_r). E, B, k, V_{ph} denote the electric field, magnetic filed, wave number, and phase velocity, respectively.

clearly demonstrates the effect of a hybrid meta-material structure (HMS) on the coupling of near magnetic field and enhancement of power transmission efficiency (PTE). Fundamentally, an HMS comprises a combination of zero permeability (μZ) and negative permeability (μNG) MMs located at the centre and edges of the HMS, respectively. While μZ straightens and focuses the outbound magnetic field from *Tx* towards *Rx*, μNG ensures the coupling and convergence of diverging flux lines at *Rx*, effectively minimizing leakage EMF and thus enhancing the PTE. As exhibited in Fig. 7, MM(s) are generally categorized as double negative (DNG)/left handed media, μ-negative (MNG) or ϵ-negative (ENG) contingent on the intrinsic properties of the medium which include the refractive index (n), effective permeability (μ_r), effective permittivity (ϵ_r), and the amplitude of magneto-inductive wave (MIW). On one hand, a DNG MM is characterized by negative effective permeability ($\mu_r < 0$) and negative effective permittivity ($\epsilon_r < 0$) consistent with backward wave propagation conditions. On the other hand, conventional materials (DPS) often referred to forward wave media exhibit $\mu_r > 0$ and $\epsilon_r > 0$ property. It should be noted that zero or near-zero permeability ($\mu \approx 0$) meta-materials enable zero refractive index and infinity phase velocity ($V_{ph} = \infty$), leading to wave propagation without any reflection and phase change whereas, $V_{ph} = 0$ for near-zero permittivity ($\epsilon \approx 0$) metamaterial [40]

Meanwhile, in deep sub-wavelength medium, the electric and magnetic field decouples, making either negative $\mu_r < 1$ or $\epsilon_r < 1$ a satisfactory condition for evanescent wave amplification in MM [41], [42]. The aforementioned presupposes that for a MM to demonstrate evanescent wave amplification, either $\mu_r < 0$ and $\epsilon_r > 0$ (μ-negative MM) or $\mu_r > 0$ and $\epsilon_r < 0$ (ϵ-negative MM) conditions must be satisfied. Besides, it is worth noting that both μ_r and ϵ_r are complex terms whose real value characterize a MM, whereas the imaginary value indicates the loss due to the leakage EMF. Thus, to qualify as a MM, the real value of either μ_r or ϵ_r or
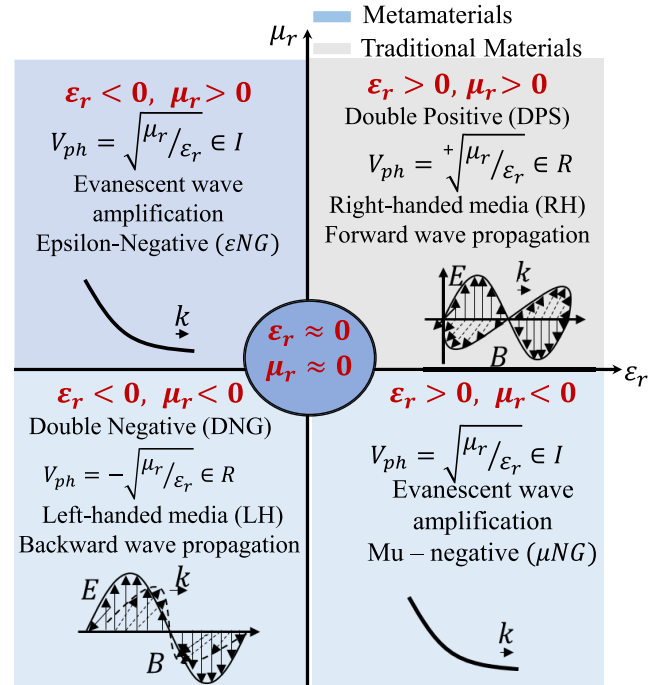
both must be negative consistent with (10).

$$n = \pm\sqrt{\mu_r \epsilon_r} \qquad (10)$$

where *n* is the refractive index of the material. For instance, a material with positive refractive index ($n > 0$) lacks the capability for evanescent amplification of near magnetic field and therefore suffers from divergence of flux lines, increased leakage EMF, and a poor performance efficiency. In the same vein, a material with negative index of refraction has both the incident and reflected waves situated in the same plane, leading to the magnetic field being confined to a common focus. The inherently enhanced capability of MM(s) in constraining and focusing outbound magnetic flux from the transmitter towards the receiver makes it an attractive candidate for mitigating leakage EMF as well as enhancing the PTE.

IV. PHYSICS BASED ANALYSIS OF METAMATERIAL (MM) BASED WIRELESS POWER TRANSFER SYSTEM
In order to fully understand the mechanism of PTE enhancement in MM-based WPT systems, various concepts, including negative refraction, Magneto-Inductive Wave (MIW) theory, magnetic dipole coupling theory, and equivalent circuit analysis have been adopted in literature [43]–[47]. Detail description of each of the theories is elucidated below.

A. NEGATIVE REFRACTION AND EVANESCENT WAVE AMPLIFICATION
In line with Maxwell's equation, the wave vector (k), electric field intensity ($\vec{E}$) and magnetic field intensity ($\vec{B}$) satisfy
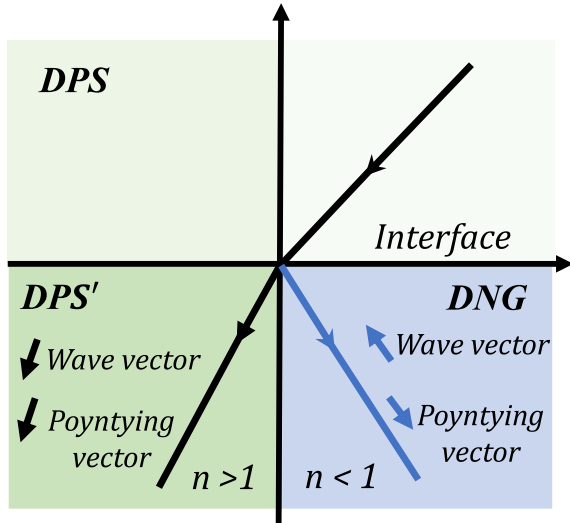
FIGURE 8. Refraction in the traditional (DPS) media and DNG (left handed) media.

the left-handed rule for MM. In accordance with [43], the expression in (10) describes the refractive index (n) of a left handed material. This implies the incident wave and the refractive wave are on the same side from the orthogonal line of the interface of the two media. On the flipside, a right handed material is characterized by $n > 0$. Based on this study, the rightness of media was introduced while ϵ_r and μ_r were extended to real number in tandem with the modified Snell's equation in (11)

$$n_1 \sin \psi = n_2 \sin \sigma = \frac{r_2}{r_1} \left| \sqrt{\frac{\mu_2 \epsilon_2}{\mu_1 \epsilon_1}} \right| \quad (11)$$

where r_1 and r_2 are the rightness of two different media; n_1 and n_2 are the refractive index of medium 1 and medium 2, respectively, ψ- angle of incidence and σ is the refractive angle of the incident wave on the MM. In general, a conventional (right-handed) and left handed MM media is defined by $r = +1$ and $r = -1$, respectively. Given that the resonant-coupling WPT depends on the near-field evanescent wave, the MM with $\mu_r < 0$ can focus the magnetic field and enhance PTE. Additionally, by exploiting the boundary conditions of the magnetic medium interface, the refraction law of the outgoing magnetic field can be expressed as:

$$\frac{\tan \psi}{\tan \sigma} = \frac{\mu_{r2}}{\mu_{r1}} \quad (12)$$

where μ_{r1} and μ_{r2} are permeability of medium 1 and medium 2, respectively. Fig. 8 denotes a pictorial depiction of the different propagation paths with respect to the *DPS* and *DNG* media.

Aside negative refraction, evanescent wave amplification is another imperative characteristic of MMs as reported by [44]. By assuming S-polarized (wave whose electric field direction is parallel to the plane of incidence) light propagating in vacuum, the associated electric field can be written as

$$\mathbf{E}_{0S+} = [0, 1, 0] \exp(ik_z z + ik_x x - i\omega t) \quad (13)$$

where the axis of the lens to the z-axis and the wave vector indicates exponential decay

$$k_z = +i\sqrt{k_x^2 + k_y^2 - \omega^2 c^{-2}}, \quad \omega^2 c^{-2} < k_x^2 + k_y^2 \quad (14)$$

Going forward, (15) shows the reflected light at the interface with the MM medium.

$$\mathbf{E}_{0S-} = r [0, 1, 0] \exp(-ik_z z + ik_x x - i\omega t) \quad (15)$$

Similarly, the electric field due to the transmitted light at the MM interface is obtained as in (16)

$$\mathbf{E}_{1S+} = m [0, 1, 0] \exp(ik'_z z + ik_x x - i\omega t) \quad (16)$$

It should be noted that

$$k'_z = +i\sqrt{k_x^2 + k_y^2 - \varepsilon\mu\omega^2 c^{-2}}, \quad \varepsilon\mu\omega t^2 c^{-2} < k_x^2 + k_y^2 \quad (17)$$

By matching the wave fields at the interface, the wave in the MM medium can decay away exponentially from the interface as seen in (18)

$$m = \frac{2\mu k_z}{\mu k_z + k'_z}, \quad r = \frac{\mu k_z - k'_z}{\mu k_z + k'_z} \quad (18)$$

On the flipside, a wave inside the MM medium incident on the interface with a vacuum can achieve transmission and reflection based on (19)

$$m' = \frac{2k'_z}{k'_z + \mu k_z}, \quad r' = \frac{k'_z - \mu k_z}{k'_z + \mu k_z} \quad (19)$$

Consequently, (20) is obtained based on the addition of multiple scattering events for calculating transmission through both surfaces of the MM medium

$$T_S = mm' \exp(ik'_z d) + mm' r'^2 \exp(3ik'_z d) \quad (20)$$

$$+ mm' r'^4 \exp\left(5ik'_z d\right) + \ldots = \frac{mm' \exp(ik'_z d)}{1 - r'^2 \exp(2ik'_z d)} \quad (21)$$

The parameter, d, in (20) symbolizes the thickness of the MM slab. Substituting (19) into (20) and taking the limit assuming $\epsilon = -1$ and $\mu = -1$ gives the transmission co-efficient as

$$\lim_{\varepsilon, \mu = -1} T_S = \lim_{\varepsilon, \mu = -1} \frac{mm' \exp(ik'_z d)}{1 - r'^2 \exp(2ik'_z d)}$$

$$= \lim_{\varepsilon, \mu = -1} \frac{2\mu k_z}{\mu k_z + k'_z}$$

$$\times \frac{2k'_z}{k'_z + \mu k_z} \frac{\exp(ik'_z d)}{1 - \left(\frac{k'_z - \mu k_z}{k'_z + \mu k_z}\right)^2 \exp\left(2ik'_z d\right)}$$

$$= \exp\left(-ik'_z d\right) = \exp\left(-ik_z d\right)$$

The corresponding reflection coefficient is given by

$$\lim_{\varepsilon, \mu = -1} R_S = r + \frac{mm' r' \exp(2ik'_z d)}{1 - r'^2 \exp(2ik'_z d)} = 0 \quad (22)$$
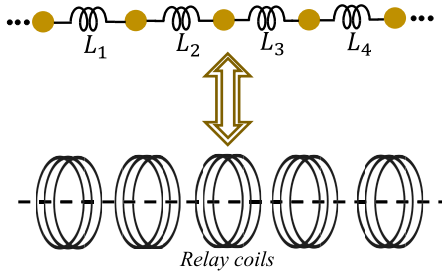
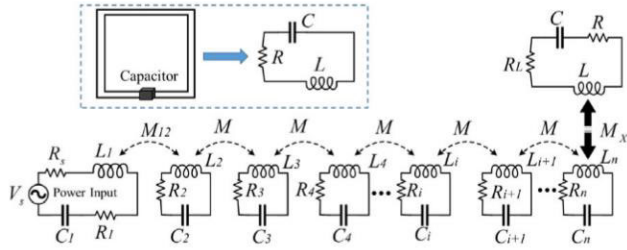**FIGURE 9.** Diagrammatic depiction of a 1-dimensional(D) MM.

FIGURE 10. Equivalent circuit model of a 1-dimensional MM.

P-polarized (electric field direction normal to the plane of incidence) evanescent waves also can be derived as follows:

$$\lim_{\varepsilon,\mu=-1} T_P = \lim_{\varepsilon,\mu=-1} \frac{2\varepsilon k_z}{\varepsilon k_z + k_z'} \frac{2k_z'}{k_z' + \varepsilon k_z} \tag{23}$$

$$\times \frac{\exp(ik_z'd)}{1 - \left(\frac{k_z' - \varepsilon k_z}{k_z' + \varepsilon k_z}\right)^2 \exp\left(2ik_z'd\right)} \tag{24}$$

$$= \exp\left(-ik_z d\right) \tag{25}$$

The above derivation clearly demonstrates the amplifying effect of MM medium on evanescent waves.

B. MAGNETO-INDUCTIVE WAVE THEORY

Based on [48], [49], the WPT based on MIW theory utilizes large number of resonating relay coils to carry signal. A popular application of MIW is found in magnetic resonance imaging. It is worth mentioning that as a form of propagation, MIWs can only be found in specific types of MMs formed based on inductively-coupled resonant circuits [45]–[47]. A schematic presentation of a typical MM based on MIW theory is shown in Fig.9. It is similar to a coupled mechanical oscillator system, which consists of a number of single-array resonators magnetically coupled via the mutual inductance between neighbouring cells. Each MM cell can be modeled as an *RLC* resonant circuit. The corresponding equivalent circuit model is exhibited in Fig. 10. Given that a current excitation in one unit cell leads to an induced current at the nearest-neighboring unit cell based on mutual coupling, the induced current causes the propagation of MIW in the MM structure. Based on the Kirchhoff Voltage Law (KVL) and mutual coupling theory, the equivalent circuit equation based

on Fig. 10 is depicted in (26)

$$\begin{cases} V_s + \left(R_s + R_1 + j\left(\omega L_1 - \frac{1}{\omega C_1}\right)\right)I_1 + j\omega M_{12}I_2 = 0 \\ j\omega M_{12}I_1 + \left(R_2 + j\left(\omega L_2 - \frac{1}{\omega C_2}\right)\right)I_2 + j\omega M_{23}I_3 = 0 \\ j\omega M_{23}I_2 + \left(R_3 + j\left(\omega L_3 - \frac{1}{\omega C_3}\right)\right)I_3 + j\omega M_{34}I_4 = 0 \\ j\omega M_{i,i-1}I_{i-1} + R_{i,i+1} + j\left(\omega L_{i,i+1} - \frac{1}{\omega C_{i,i+1}}\right)I_i \\ \qquad\qquad\qquad +j\omega M_{i,i+1}I_{i+1} = 0 \\ j\omega M_{n,n-1}I_{n-1} + \left(R_n + R_L + j\left(\omega L_n - \frac{1}{\omega C_n}\right)\right)I_n = 0 \end{cases} \tag{26}$$

where V_s is the source voltage, R_s is the internal resistance of the source; R_i, L_i and C_i are the equivalent resistance, self-inductance and capacitance of the unit cell, respectively, whereas M_{ij} describes the mutual-inductance between two adjacent coils. Meanwhile, the current in each unit cell of the MIW waveguide due to the wave travelling in the MM is expressed as seen in (27)

$$I = I_o^{-\gamma nd} = I_o e^{-(\alpha + j\beta)nd} \tag{27}$$

where α is the attenuation constant which represents the wave reduction along the MM, γ is the propagation constant, d symbolizes the period of the cells and n refers to the nth unit cell. Moreover, the attenuation of the MIW in each unit cell can be expressed by the dispersion equation

$$\alpha d = \sin h^{-1}\left(\frac{1}{\eta \kappa_c Q}\right) \tag{28}$$

where η is the number of spatial dimensions occupied by the lattice, αd is the attenuation per cell for MIW transmission, Q is the quality factor, κ_c is the coupling coefficient evaluates as $\kappa_c = \frac{2M}{L}$, whereas M and L are the mutual inductance between the MM structure and the self-inductance of the MM, respectively. Furthermore, the phase factor, β can be expressed as

$$\beta = \frac{1}{a} \arccos\left(\frac{\omega_0^2/\omega^2 - 1}{2\kappa_C}\right) \tag{29}$$

where a is the distance between the unit cells. It is conspicuous based on (28) that for efficient power transmission in this medium, strong coupling (high κ_c) and low loss (high Q) resonators are preferred. Hence, in order to realize optimal MM power transfer designs, the figure of merit should be maintained as high as possible. In addition, the transmission efficiency based on MIW theory can be obtained by combining both the forward (S_{21}) and reverse (S_{11}) scattering parameters as shown in (30)

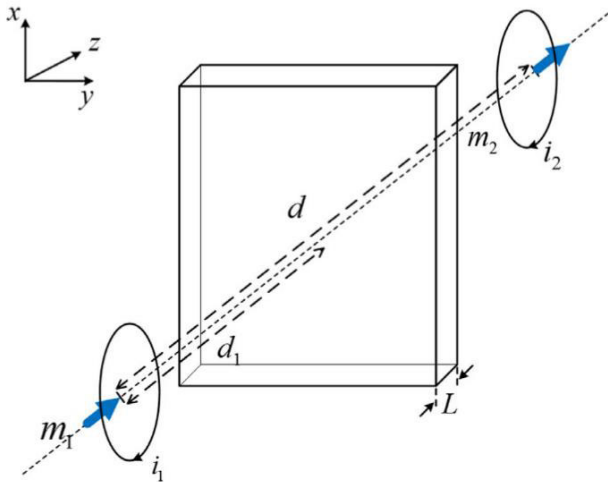$$\eta_{power} = \frac{s_{21}^2\left(1 + \frac{Z_O}{R_L}\right)}{1 - s_{11}^2} \tag{30}$$

FIGURE 11. Pictorial representation of magnetic dipole based on the MM slab.

(a) Schematic of the proposed unit MM structure

(b) Four coil WPT structure incorporating a MM-slab (3×3 array of unit cell)
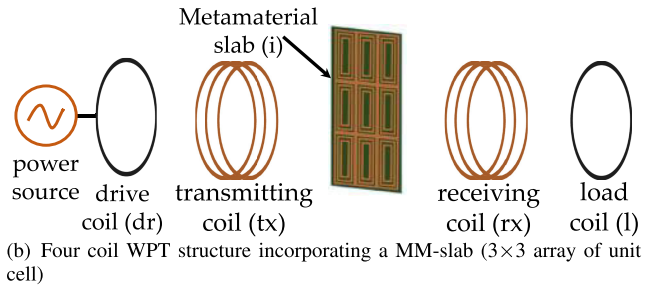
FIGURE 12. MM unit cell, equivalent lumped circuit model, four coil WPT system incorporating an MM slab.

where Z_o is the characteristic impedance and R_L is the load resistance across which the output is measured. In practice, both S_{21} and S_{11} can be measured with vector network analyzer. A comprehensive theoretical investigation of the MIW theory in MM-based WPT systems is elucidated in [27], [50].
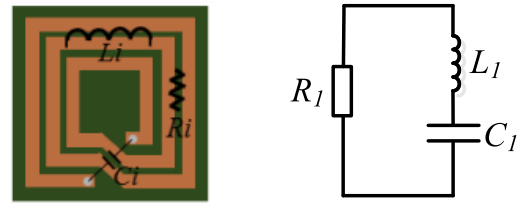
C. MAGNETIC DIPOLE COUPLED MODE THEORY

The concept of couple mode theory has been discussed explicitly in [51]. As shown in Fig. 11, the proposed structure is based on a simplified model of a magnetic dipole, comprising two single-turn coils coupled through a homogeneous medium. The medium will affect the mutual inductance between the magnetic dipoles as well as self-inductance. If the medium is composed of a MM with special EM constitutive parameter tensors, then in theory, the MM can be designed to realize a complete coupling of two different magnetic dipoles. Exploiting this strategy, the mutual inductance based on two magnetic dipoles with and without MM structure has been modeled as shown in

$$M_{21}^{vac} = \frac{\mu_x \mu_o F_1 F_2}{4\pi} \phi_L\left(0, 3, \frac{d}{2D}\right) = \frac{\mu_x \mu_o F_1 F_2}{4\pi d^3} \quad (31)$$

$$M_{21} = \frac{\mu_x \mu_o F_1 F_2}{4\pi} \frac{h}{a(2\alpha D)^3} \phi_L\left(\frac{-b}{a}, 3, u\right) \quad (32)$$

where F_1 and F_2 denotes the area of magnetic dipole, μ_v- relative permeability of the homogeneous medium in which the magnetic dipole is located, d is the distance between the magnetic dipoles evaluated as $d = D + d_1 + d_2$, α typifies the anisotropic ratio of the MM constitute parameter described by the expression, $\alpha = (\frac{\mu_x}{\mu_z})^{\frac{1}{2}}$. whereas the constants a, b and h of the MM are given by the expression (33)-(35)

$$a = \left(\left(\frac{\alpha}{\mu_x}\right) + \left(\frac{1}{\mu_v}\right)\right)^2 \quad (33)$$

$$b = \left(\left(\frac{\alpha}{\mu_x}\right) - \left(\frac{1}{\mu_v}\right)\right)^2 \quad (34)$$

$$h = \left(\frac{4\alpha}{\mu_x \mu_y}\right)^2 \quad (35)$$

Besides, the function ϕ_L can be expressed as

$$\phi_L(z, s, \alpha) = \sum \frac{z^n}{(n+\alpha)^s} \quad (36)$$

While the influence of MM on the self-induction of magnetic dipoles is negligible in comparison to the mutual inductance, it should be stated that by calculating the ratio of M_{21} to M_{21}^{vac}, the degree of coupling between the two magnetic dipoles can be enhanced by the MM.

D. EQUIVALENT LUMPED CIRCUIT MODEL OF MM-BASED WPT SYSTEM

The concept of equivalent circuit models has been harnessed in various literature to emulate the behavior of a MM-based WPT systems [52]–[54]. Moreover, numerical analysis based on equivalent circuit representation of these systems have also been explored to evaluate their transfer characteristics and power transfer efficiency. While the earlier discussed approaches, including MIW theory and magnetic coupled mode theory have been exploited to explain the physics of MM-based WPT systems, some of the reactive parameters and the basic physical interpretation have not been clearly expounded. Equivalent circuit approach focuses on the effect of the system parameters and transfer coils on the system transfer characteristics and its effectiveness in analyzing complex circuit. In general, most studies of the MM-based WPT system focus MHz frequency range for consumer electronics. The wavelength of current is far larger than the system dimension, including MM slab and size of the resonant coils. Based on this, it can be assumed that the current flowing in each part is identical and in phase and the whole system can
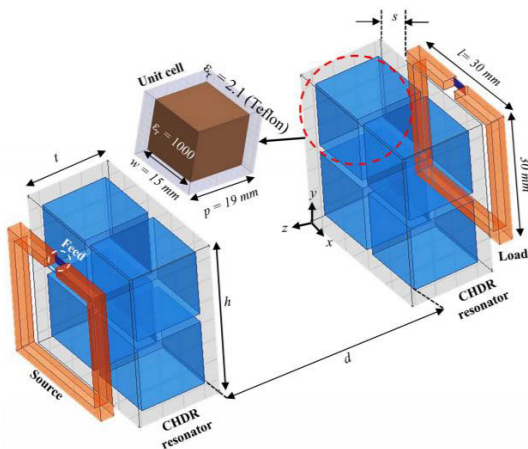
FIGURE 13. Equivalent circuit schematic of the proposed four coil metamatarial(MM)-based WPT system. The comprises a 3 × 3 periodic array of MM unit cell in Fig. 13(a).

be viewed as lump circuit model, in which the distribution of the parameters are ignored. In consonance with [55], each unit cell of the MM can be modeled as a resistance-inductor-capacitor (RLC) resonant circuit exhibited in Fig. 13(a) where $L_i(i = 1, 2, 3\ldots.9)$, $C_i(i = 1, 2, 3\ldots.9)$, and $R_i(i = 1, 2, 3\ldots.9)$ are the lumped circuit inductance, capacitance and resistance of the unit cell, respectively. Notice that the subscript *i* indicates each unit cell in the MM-slab. As shown in (37), the resistive component consists of the ohmic loss (R_o) and dielectric loss (R_d) due to the copper coil

$$R_i = R_o + R_d \tag{37}$$

Similarly, the capacitive component can be described as the sum of the stray capacitance (C_s) and compensation capacitor C_p as demonstrated in (38)

$$C_i = C_s + C_p \tag{38}$$

It is worth stating that the resonant operating frequency of the MM-based WPT structure can be adjusted by varying the value of the compensation capacitor, C_p, accordingly. Based on the aforementioned, the performance of the proposed MM-based WPT system can be effectively optimized by tuning the value of C_p. Further, the MM-slab between the transmitting and receiving coil in Fig. 13(a) consists of a 3 × 3 array of the unit cell in Fig. 13(b). Intuitively, such a loosely disconnected array of cells can be considered as a multiple repeater coils or booster network for achieving evanescent wave amplification of near magnetic field as well as increasing the amount of power transfer. Using KVL and coupling theory, the circuit equations of the MM-based WPT system can be analyzed as showcased in (39).

$$\begin{cases} Z_{tx} = R_{tx} + j\left(\omega L_{tx} - \dfrac{1}{\omega C_{tx}}\right) \\[2mm] Z_{rx} = R_{rx} + j\left(\omega L_{rx} - \dfrac{1}{\omega C_{rx}}\right) \\[2mm] Z_{dr} = R_{dr} + j\left(\omega L_{dr} - \dfrac{1}{\omega C_{dr}}\right) \\[2mm] Z_l = R_L + R_l + j\left(\omega L_L - \dfrac{1}{\omega C_L}\right) \\[2mm] Z_i = R_i + j\left(\omega L_i - \dfrac{1}{\omega C_i}\right) \end{cases} \tag{39}$$

where $\omega = 2\pi f_r$ and f_r is the resonant operating frequency. Further, the current flowing through each of the resonant circuit and MM unit cell can be evaluated by applying Kirchoff's Voltage Law (KVL) and coupling theory to the equivalent circuit in Fig. 13.

$$\begin{aligned} V_s = {} & I_{dr}(R_s + Z_{dr}) + j\omega M_{drtx}I_{tx} + j\omega M_{dr1}I_l + j\omega M_{dr2}I_2 \\ & + \ldots j\omega M_{dr9}I_9 + j\omega M_{drtx}I_l \end{aligned} \tag{40}$$

$$\begin{aligned} 0 = {} & I_{tx}Z_{tx} + j\omega M_{drtx}I_{dr} + j\omega M_{tx1}I_1 + j\omega M_{tx2}I_2 \\ & + \ldots j\omega M_{tx9}I_9 + j\omega M_{txL}I_L \end{aligned} \tag{41}$$

$$\begin{aligned} 0 = {} & I_iZ_i + j\omega M_{dri}I_{dr} + j\omega M_{tx1}I_1 + j\omega M_{tx2}I_2 \\ & + \ldots j\omega M_{tx9}I_9 + j\omega M_{il}I_i \end{aligned} \tag{42}$$

$$\begin{aligned} 0 = {} & I_l(R_L + Z_l) + j\omega M_{dri}I_{dr} + j\omega M_{txl}I_{tx1} + j\omega M_{tx2}I_2 \\ & + \ldots j\omega M_{tx9}I_9 + j\omega M_{il}I_i \end{aligned} \tag{43}$$

Converting the expressions (40), (41), (42) and (43) to matrix form gives

$$\begin{bmatrix} V_S \\ 0 \\ 0 \\ \vdots \\ 0 \end{bmatrix} = \begin{bmatrix} R_s + Z_{dr} & jwM_{drtx} & jwM_{dri} & \cdots & jwM_{drl} \\ jwM_{drtx} & Z_{tx} & jwM_{txl} & \cdots & jwM_{txl} \\ jwM_{dri} & jwM_{txi} & Z_1 & \cdots & jwM_{il} \\ \vdots & \vdots & \vdots & & \vdots \\ jwM_{drl} & jwM_{tl} & jwM_{iI} & \cdots & R_L + Z_l \end{bmatrix}$$
$$\times \begin{bmatrix} I_{dr} \\ I_{tx} \\ I_i \\ \vdots \\ I_l \end{bmatrix} \tag{44}$$

Considering the weak coupling between non-adjacent coils, the mutual inductance, $M_{dri}, M_{txrx}, M_{il}, M_{drl}$ is assumed to be zero as in (45)

$$M_{dri} = M_{txrx} = M_{il} = M_{drl} = 0 \tag{45}$$

V. LITERATURE REVIEW

Numerous literature have reported the utilization of MM for performance enhancement of WPT systems. In [56], [57], the incorporation of MM slabs with conventional two coil and three coil WPT structures is presented. Concretely, the efficient performance of MM in a WPT system depends on its ability to enhance evanescent wave amplification of near magnetic field, a phenomenon that is largely influenced by the polarity of medium parameters, including μ_r, ϵ_r and *n*. In practice, MM-based WPT system can be designed by placing one or more MM slab in between a *Tx* and *Rx* coil, essentially generating the required excitation as well as channeling the flux lines towards the receiver. It is worth noting that an MM slab can be fabricated by creating periodic arrays and layers of the proposed MM unit cell. In addition, their categorization is based on spatial orientations as evident in the 2-D planar [58], [59] and 3-D volumetric double negative (DNG) [60] MMs and material composition, including zero-negative and μ-negative-zero (μNZ) MM. Generally, 2-*D* planar DNG MM(s) are primarily

FIGURE 14. Schematic of high power CHDR MM-based WPT system [66].

implemented as transmission line and can be designed either as a lump or distributed circuit. Additionally, its adoption has proven highly efficient in synthesizing negative index designs for different types of applications [53], [58], [59], [61]–[63]. In addition, 3-D volumetric DNG MM(s) are formed by embedding small artificial inclusions (wires, split ring resonators etc.) in the host media [60], [64]. A 180 × 180 mm^2 one-sided 3 × 3 MM slab based on a 60 × 60 mm^2 μ-negative-zero (μNZ) unit cell has been exploited in [65] to enhance the PTE of a WPT system. Performance analysis of the system with the proposed MM slab results in a PTE of 55.3%, indicating an improvement of 15.7% compared to a wireless power transfer system without the MMs. The uniqueness of this design is rooted in the fact that it demonstrates a continuous improvement in PTE even with increasing transfer distance.

A. HIGH DIELECTRIC/PERMITTIVITY MM BASED WPT

In [68], realization of single/double negative MM using high dielectric materials is introduced. Besides, theoretical analysis of a negative MM design based on high dielectric sphere proposed in [69], [70] coupled with a cylindrical MM [71] based on Mie resonance theory [72] has been studied. Mie resonance theory simply describes the creation of resonant electric and magnetic field while offering different pathways for the fabrication of MMs [72]. Further, [66] proposed a two coil WPT system incorporating a pair of 2 × 2 array of a cubic high dielectric resonator (CHDR) MM structure as denoted in Fig. 14. The CHDR MTM resonators are placed in front of the source and load coils with a distance of 4 mm. To validate the theoretical approximation, an ANSYS HFSS model based on the proposed unit MM cell is established, as shown in Fig. 15. Using finite-element solver of HFSS, the resonant frequency, f_o was calculated under normal incidence and the resulting extracted medium parameters, including effective permittivity (μ_r), effective permeability and refractive index (n) are calculated based on the transmission and relection scattering parameter (S_{11}, S_{21}), and impedance as shown in

(a) Side view of the fabricated antenna

(b) Measured and simulated scattering parameter
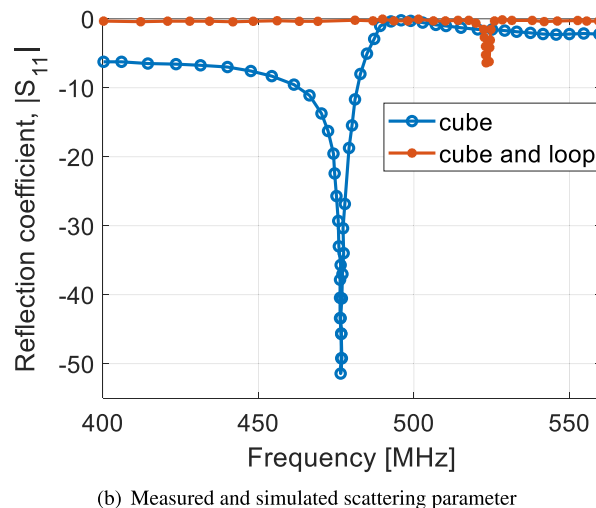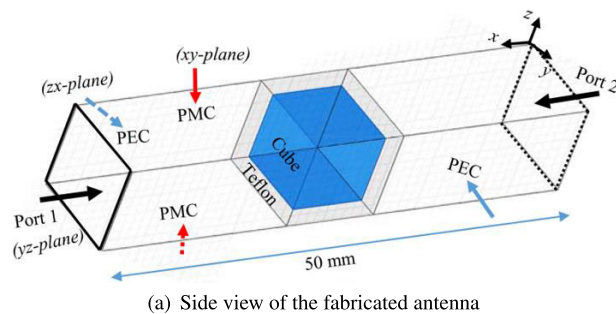
FIGURE 15. (a) Side view of the proposed antenna. Dimensions are in mm (b) Measured and simulated S-parameter of the proposed antenna showing resonant frequency peak [67].

(46), (47) and (48), respectively.

$$z = \pm\sqrt{\frac{(1 + S_{11})^2 - S_{21}^2}{(1 - S_{11})^2 - S_{21}^2}} \quad (46)$$

$$e^{\text{ink}_o d} = \frac{S_{21}}{1 - S_{11}[(z - 1)/(z + 1)]} \quad (47)$$

$$\varepsilon_r = n/z \quad \text{and} \quad \mu_r = n \cdot z \quad (48)$$

It should be noted that $e^{\text{ink}_o d}$ is an exponential term which consists of the refractive index, n, MM thickness, d, and wave number, k_o, evaluated as $\frac{2\pi}{\lambda}$ where λ is the electromagnetic wavelength. In addition, the magnitude of $e^{\text{ink}_o d}$ is always smaller or equal to 1, which guarantees that the sign of the imaginary part of n will be correct based on (49)

$$n = \frac{1}{k_o d}(-ie^{\text{ink}_o d} + 2m\pi) \quad (49)$$

where m is an integer. It is worth mentioning that both μ_r and ϵ_r in (48) are extracted by exploiting the standard kramar kronig retrieval algorithms as exemplified in [69], [70], [72]. The real and imaginary plots of μ_r and ϵ_r, showing multiple resonant frequency peaks are shown in Fig. 16. In order to provide current excitation, the transmitter (exciting coil) is connected to a voltage source while placing the transmitter and receiver (load coil) directly behind individual
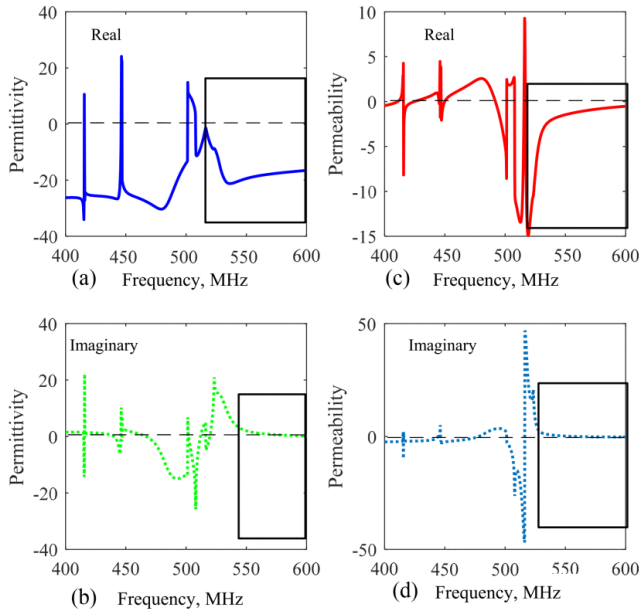
FIGURE 16. Extracted Parameters of the CHDR structures showing multiple resonant peaks (a) Real effective permittivity (b) Imaginary effective permittivity (c) Real effective permeability (d) Imaginary effective permeability [66].

CHDR slab as shown in Fig. 14. Further, Fig. 17 shows the simulated transmission scattering parameter and efficiency of the model based on ANSYS HFSS analysis. The resulting simulated and measured resonant frequencies are obtained as 476.8MHz and 1.7GHz, respectively. The disparity in the value of simulated and measured frequency is attributed to the differences in the material and size of the CHDR MM resonator. While the WPT design demonstrates high dielectric permittivity coupled with a PTE of 52% at a transfer distance of 360*mm*, its high resonance frequency presents a major challenge to power electronic and semiconductors given that high frequency increases the turn ON and turn OFF time of power MOSFET, leading to high power dissipation and switching losses. The vector distribution of the magnetic field, $\vec{H}$ and Electric field, $\vec{E}$ are plotted as shown in Fig. 17(b) and Fig. 17(c), respectively. Essentially, both $\vec{E}$ and $\vec{H}$ are strongly confined in each cube located inside the CHDR with $\vec{E}$ swirling inside a CHDR cube while $\vec{H}$ lies orthogonally to $\vec{E}$ as well as penetrates in and out of the CHDR structure. This behavior is consistent with MIE resonance [72] which stipulates that under proper excitation, a high refractive index dielectric exhibits a strong magnetic resonance. The influence of increasing the number of arrays of the unit cell on power loss mitigation, evanescent wave amplification and efficiency enhancement is investigated by comparing the measurement results of two identical 3 × 3 CHDR MTMs having dimensions 53 × 53 × 19(mm^3), loop thickness 0.5*mm*, a separation distance, *d* and excited by two similar rectangular loops of dimensions 50 × 50 mm^2 is shown in Fig. 18. Besides, the practical size of the CHDR MM structure is too large to be incorporated in WPT systems. The region covered by the blue rectangular box is the negative
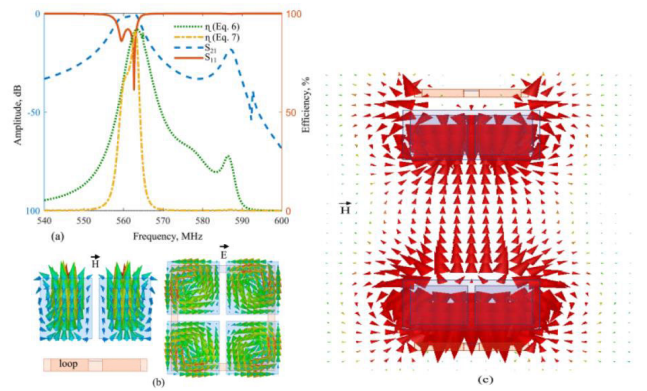
FIGURE 17. (a) Characteristics of the proposed WPT system in terms of η, S_{11}, and S_{21}. (b) Magnetic ($\vec{H}$) and electric ($\vec{E}$) field distributions of the MM-coupled WPT system. (c) Horizontal magnetic ($\vec{H}$) dipole mode coupling for the proposed WPT system. [66].

refractive index region. In this region, the real values of both ϵ_r and μ_r are negative. Therefore, the CHDR MM resonator realizes the properties of the DNG MMs in this region. As for the implementation of the CHDR MM-based WPT system, the CHDR cube has been fabricated using the EXXELIA TEMEX E5080 ceramic ($\epsilon_r = 78$). The entire CHDR MM consists of a 3 × 3 array and is excited by the source and load coils. The measured resonant frequency of the CHDR based WPT system is 1.7 GHz which is higher in comparison to the simulated due to disparity in the material and size of the CHDR MM resonator. In [73], a compact low-loss circular spiral split ring resonator based on high permittivity is proposed. The planar structure of the unit cell in Fig. 19(a) meant its length scale is small at the operating wavelength, essentially ensuring it does not present the design limitation associated with bulky structures while also eliminating the complexity of non-planar configurations [16]. The complete WPT set-up consists of a two 2 × 2 HP spiral-split ring MM slabs each located in front of a source and load coil and separated by a distance d_g taken as 30*mm* as shown in Fig. 19(b). In a pattern similar to [66], the MM was simulated in ANSYS HFSS to extract the simulated scattering parameters which is then inserted in Kramer-Kronig retrieval algorithm to evaluate the values of μ_{eff} and ϵ_{eff}. The real part of μ_f is high (681.4) whereas the imaginary component is 0.47, indicating a low leakage magnetic flux in the MM all while resonating at a frequency of 469.4MHz as evident in the MM S-parameter and effective permittivity plot in Fig. 20 (a) and Fig. 20(b), respectively.

Experimental test-bed for the measurement of the model's medium parameters coupled with the WPT efficiency under varying transmitter to MM distance is demonstrated in Fig. 21. By varying the transfer distance, d, the efficiency and S-parameters of the WPT system were measured with and without the proposed MM. Subsequently, a comparative analysis of the simulated and measured S-parameter and power transfer efficiency (PTE) of the system with MM and without MM was investigated as presented in Fig. 20 and Fig. 22, respectively. Based on the obtained
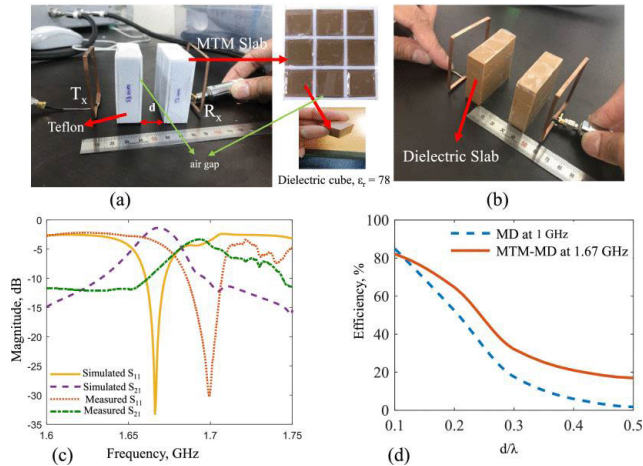
FIGURE 18. (a) Experimental set-up for measuring scattering parameters and efficiency [66]. (b) Schematic of the magnetic dipole (MD)-based WPT system. (c) Simulated and measured S_{11} and S_{21} for the proposed WPT system at 0.1λ. (d) Variation in efficiency due to the working distance for the MTM-MD and MD-based WPT systems.
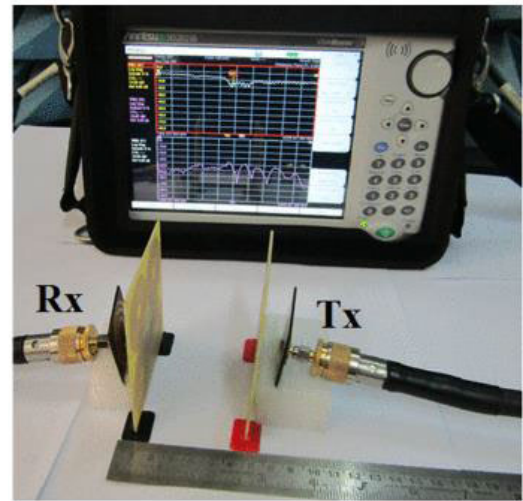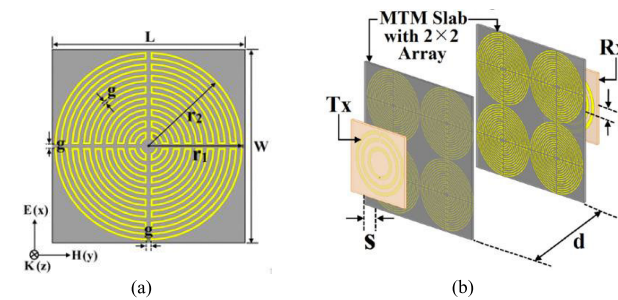

FIGURE 19. (a) Schematic configuration of the MTM unit cell, where $L = W = 40$ mm, $r_1 = 19.8$ mm, $r_2 = 19.5$ mm, and $g = 0.7$ mm. (b) Geometry of the proposed WPT system with MTM slabs [73].
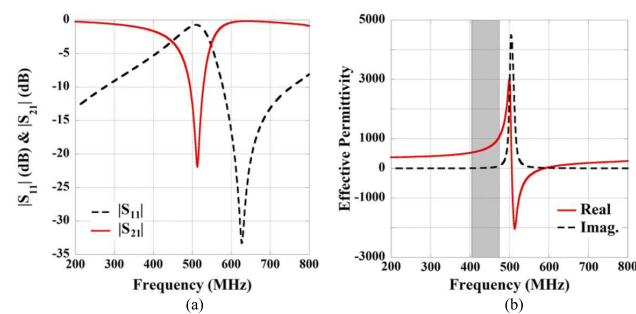
FIGURE 20. (a) Extracted reflection (S_{11}) and transmission (S_{21}) S-parameters of the MM unit cell. (b) Retrieved real and imaginary parts of effective permittivity [73].

wave-forms, the simulation and measurement efficiencies improved by 8.6% and 9.1%, respectively when the MM slab is inserted in the WPT system. Low PTE is indicative of system high power dissipation and equally represents a metric for gauging the reliability of a wireless power transfer system. The smallish value of PTE can be attributed to the reduction in amplitude of evanescent wave coupled with high resonant frequency of the MM. In practice, high power WPT application thrives best under low frequency excitation. This finds explanation in the fact that low frequency mitigates the effects of parasitic impedance, which if appreciable could

FIGURE 21. Experimental test-bed for measurement of PTE and S-parameter [73].
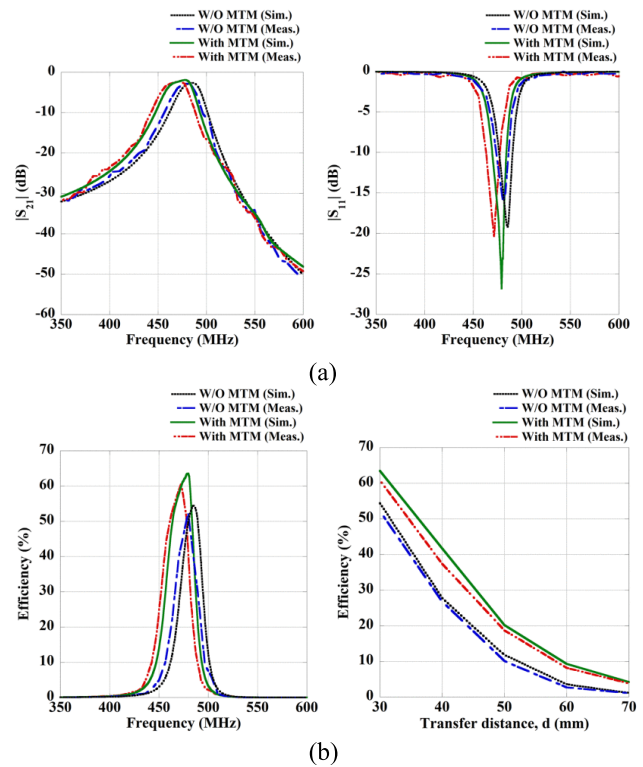
FIGURE 22. Plot of simulated and measured S-parameters with and without MM [73].

prove counter-productive to the overall performance of the WPT system.

B. MINIATURIZED LOW FREQUENCY MM-BASED WPT TOPOLOGIES

In-spite of the capability of MMs in improving the performance of WPT systems over wide transfer distance, there are obvious limitations in its utilization including concerns with reliability and power dissipation caused by the high resonant
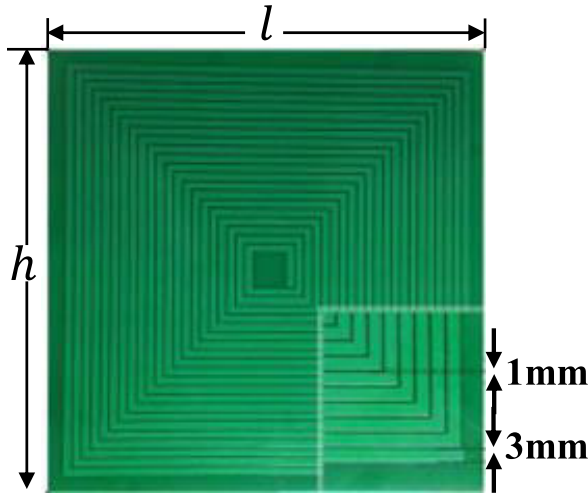
(a) Proposed MM
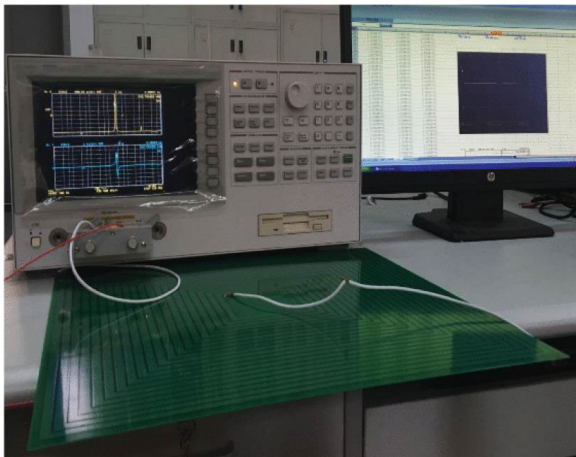
(b) Prototype set-up

FIGURE 23. **(a) Proposed square shaped unit cell (b) Experimental set-up [74].**

FIGURE 24. **Schematic of high power CHDR MM-based WPT system [74].**

operating frequency of existing MMs. Over the years, effort has been directed at optimizing current high frequency MMs as well as presenting novel designs for high power WPT applications. In [74], an in-depth analysis and design of kHz-MM-based WPT is elucidated. Parameter optimization based on tuning the number of turns/layers of unit cell and inter-turn spacing was utilized to adjust the MM parasitic capacitance (C) and parasitic inductance (L), respectively. Using the Swiss roll design in Fig. 23(a) as a case in point and considering the tuning of its model parameters based on the resonance frequency, $f_o = \frac{1}{LC}$, the MM is observed to resonate at a frequency, $f_o = 10.282$MHz based on measurement taken with vector network analyzer (VNA) as shown in Fig. 23(b).

Nonetheless, it is observed that by optimizing the design parameters of the MM represented in Fig. 23(a), including the inter-turn spacing, line to gap ratio etc. In accordance with the flowchart in Fig. 24, the resonant frequency, f_o is reduced from 10.282MHz to 821.3kHz, effectively ascertaining that f_o can be minimized by maximizing the parasitic inductance

and parasitic capacitance of the proposed structure. Upon the implementation of the optimization algorithm, an experimental comparative analysis of the measured μ_r and ϵ_r based on Agilent 4924A VNA with and without optimization of design parameters is shown in Fig. 25(a) and Fig. 25(b), respectively. Additionally, using the optimization algorithm, a parametric sweep of design parameters based on a variation of the number of layers of the metastructure coupled with an increase in the number of layers of the proposed unit cell is investigated to understand the impact of tuning design parameters on the behavior of proposed unit cells. The resulting simulation results are presented in Fig. 26(a) and Fig. 26(b), respectively. Fig. 26(a) shows that by maintaining a constant line width and increasing the inter-turn spacing, the resonant frequency, f_o is further reduced from 821.28MHz to 750kHz, 850kHz and 950kHz, corresponding to a line to gap ratio 3/0.5(mm), 3/0.75(mm), and 3/1(mm), respectively. Similarly, Fig. 26(b) reveals the influence of varying the number of layers of unit MM on the evanescent wave characteristics and left-handed behavior of the structure. For the same variation and line width and inter-turn spacing, the proposed model behaves as an evanescent wave amplifier for two layers of MM cells while exhibiting right-handed characteristics when changed to 1 and 4 layers. This is evident from the real values of effective permeability of proposed model which is negative for double layers and positive for
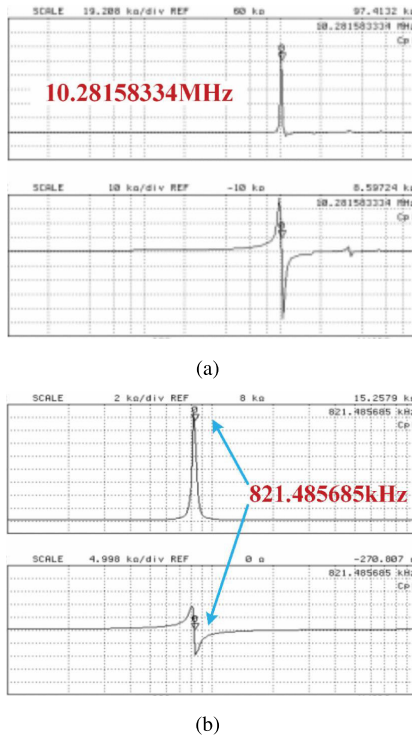
(a)

(b)

FIGURE 25. (a) Measured results of the non-optimized design (b) Measured results of the optimized design [74].

TABLE 1. Comparison of resonant frequency for different substrate material and similar slab size.

Material	Dielectric Constant	Slab size	Frequency (MHz)
Aluminium	1.0	240 × 240 × 3	-
Bitumen	3.9	240 × 240 × 3	20.3
Cyanate	4.3	240 × 240 × 3	20.4
Glass	5.5	240 × 240 × 3	19.0
Silicon	11.9	240 × 240 × 3	16.4
Diamond	16.5	240 × 240 × 3	13.9

single and triple layers. Similarly, the paper investigates the impact of substrate material, dielectric permittivity and loss tangent on the operating resonant frequency of the MM-based WPT structure. In accordance with Table 1, it is observed that for the same MM dimensions and considering different substrate material, the f_o decreases with increasing dielectric constant and decreasing loss tangent. It is worth mentioning that the dielectric constant of a material depends on its internal structure and material compositions. While the resonant frequency of the design has been significantly reduced based on the proposed optimization routine, its value is still very large, especially when compared to the $85kHz$ operating frequency high power WPT applications.

The study conducted in [42] proposed a compact low frequency ferrite loaded MM for enhancing the efficiency of a WPT system. The study harnessed a ferrite loaded solenoid with a size 1/10000 of the electromagnetic wavelength as the unit cell based on Fig. 27(a). By leveraging the electromagnetic boundary conditions and assigning wave-guide port
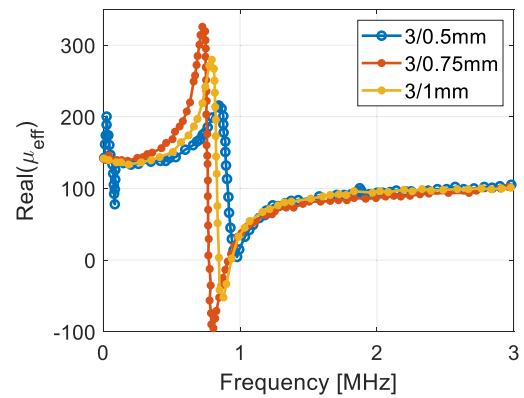
(a) Impact of ratio of line width to the gap
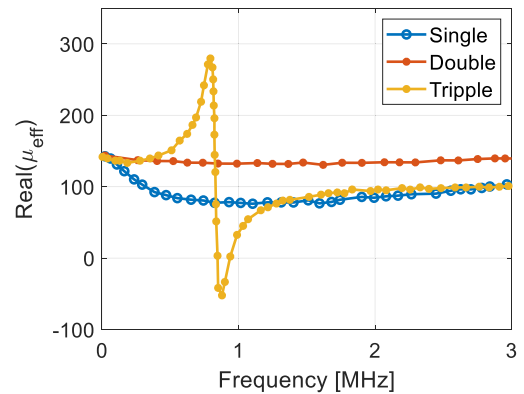
(b) Impact of the number of MM layers

FIGURE 26. Permeability curve showing impact of the (a) ratio of line width to the gap (b) number of layers [74].

in a full wave HFSS simulation, the S_{11} and S_{21} parameter of the unit cell was extracted while also retrieving the effective permeability and effective permittivity of the MM using a method proposed by Smith et al [75]. The retrieval algorithm culminates in a negative real effective permeability ($\mu_r = -1$) and resonant frequency, $f_{res} = 5.36MHz$, as denoted in Fig. 28(b), effectively characterizing the design of the MM. It is worth noticing that the relatively small value of the simulated resonant frequency of the structure compared to that of RF and microwave based MM makes a preferred choice for high power application. For the prototype implementation, a 77 Ferrite loaded unit-cell sample with dimensions of $600\,mm \times 600mm \times 200\,mm$ was fabricated as shown in Fig. 28(a) while the impact of varying the extraction distance ($6mm$, $8mm$, and $10mm$) on the material's relative permeability is depicted in Fig. 28(b). As the extraction distance increases, a characteristic frequency shift/reduction in the effective material properties is observed, underlining a strong resonance coupling with closely spaced unit cells, but also to the inter-cell coupling and by extension, increase the efficiency enhancement of the system. For mutual impedance measurements only, a 40Ω resistor was added to the coils in series in order to provide a broadband impedance match that would not affect the frequency response of the system.
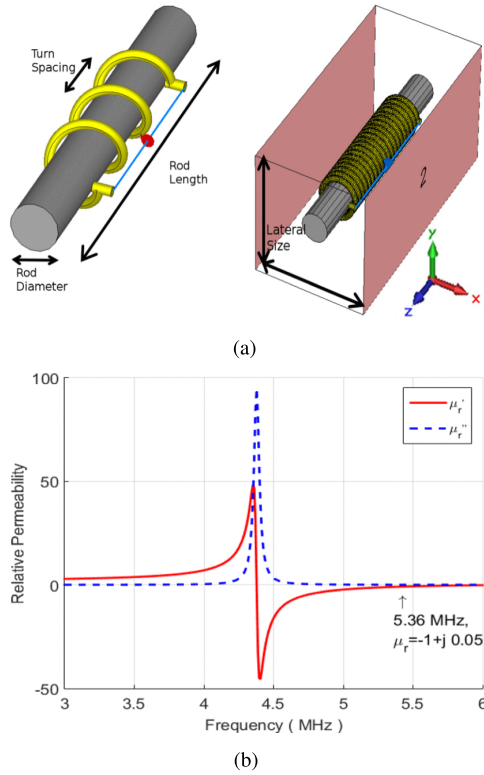
(a)

(b)

FIGURE 27. (a) Schematic of a unit MM cell as designed in HFSS (b) Effective Permeability of the proposed unit cell [42].
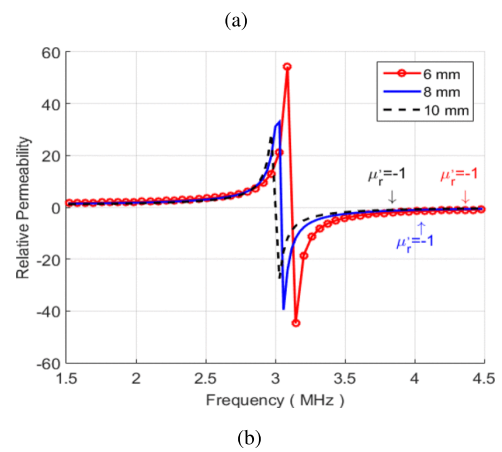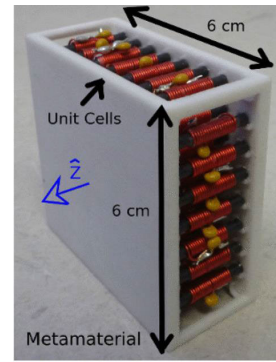

(a)

(b)

FIGURE 28. (a) Prototype/Fabricated compact MM structure (b) Effective permeability of the proposed unit cell [42].

**TABLE 2.** Comparison of metamaterial (MM) resonant frequency for different substrate material [76].

Substrate type	Dielectric Constant	Frequency band (GHz)	MM
Rogers RT-6010	10.2	2.36–2.63; 3.33	DNG; ENG
Aluminum nitride	8.6	2.39, 3.33; 3.55	ENG; MNG
FR-4	4.2	3.45; 3.6	ENG; NZRI
Poly-amide	3.5	3.6–3.7	DNG

This effectively reduces the effect of measurement noise, achieves maximum power transfer while also improving the PTE. Fig. 29(b) shows the waveform of the mutual impedance based on the measurement set-up in Fig. 29(a). The large enhancement in mutual impedance seen around 5.574 MHz is particularly notable. Another conspicuous observation is the dependence of mutual impedance on resonant frequency, which is expected since the effective material properties of the sample changes with frequency. Additionally, it is revealing that the maximum value of mutual impedance is achieved at an excitation frequency 5.574 MHz different than that of the unit-cell (3.35MHz – 3.50 MHz). This can be attributed to the fact that negative permeability is achieved above resonance and results in mutual impedance enhancement. A comparative analysis of the variation in mutual impedance, Z_M of the MM with the receiver radius and transmitter to receiver coil spacing is shown in Fig. 30(a) and Fig. 30(b), respectively. With reference to the waveform in Fig. 30(a), a 5Ω and 0.1Ω peak mutual impedance is observed corresponding to circuit simulation with MM and without MM, respectively. In the same vein, Fig. 30(b) shows a close matching of the measurement and simulation results Z_M for both air and MM media. In spite of the compact structure of the proposed MM, its operating resonant frequency is too high compared to the conventional WPT frequency based on SAE standard which stipulates an 85kHz resonant frequency for optimal WPT system performance. To minimize power dissipation while operating at the

resonant frequency of the MM (5.36MHz), a zero switching technique can be implemented to mitigate the switching losses and dead time occasioned by the multiple switching transitions of the semiconductors in power electronic circuit.

Similarly, in [76], the effect of substrate material on the electromagnetic wave/left-handed characteristics of the MM-based WPT system is investigated and the corresponding resonance frequency for different substrate material is presented in Table 2. Initially, the unit cell of the MM was designed on FR-4 substrate resulting in 3.45*GHz* resonant frequency. However, further analysis based on the replacement of FR4 substrate with different substrates, including Rogers RT 6010, lossy polyamide and Aluminum Nitride, each having the same dimension as FR4 but different dielectric loss-tangent and dielectric constant leads to the realization of left handed (double negative) features within the same frequency band. Besides, simulation results show that Roger
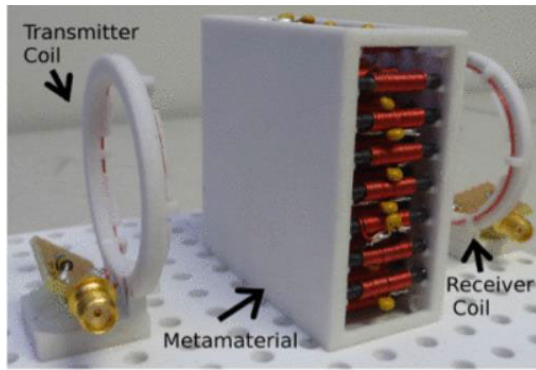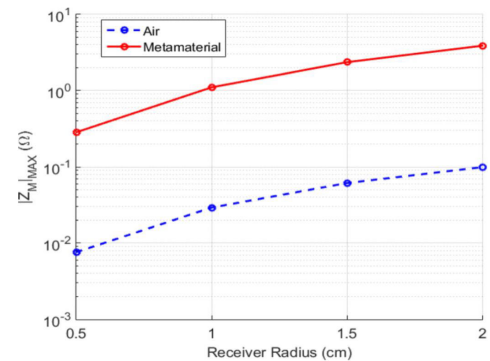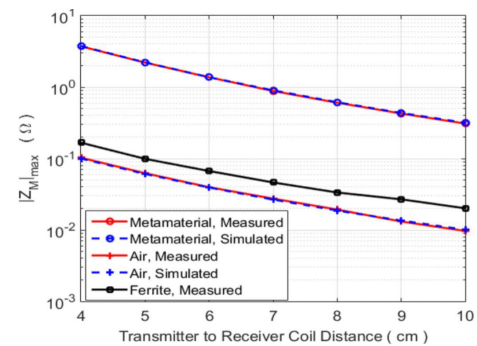
(a)
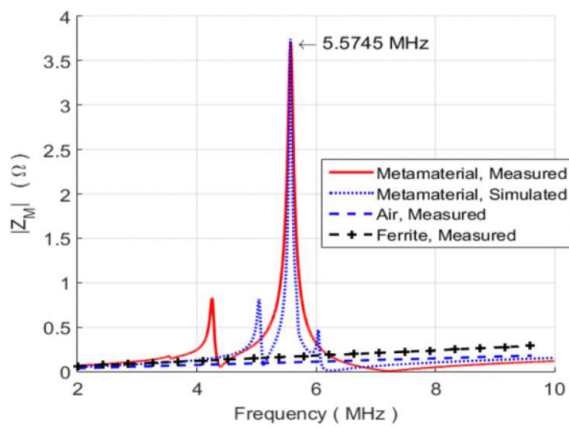
(b)

FIGURE 29. (a) Mutual impedance measuring setup. (b) Measured mutual impedance between two coils that are 400*mm* apart. [42].

(a)

(b)

FIGURE 30. (a) Comparison of measured mutual Impedance, Z_M with and without MM (b) Comparison of measured and simulated Z_M with MM and without MM [42].

RT 6010, Poly-amide and Aluminum Nitride substrate materials demonstrate resonant frequencies 2.36GHz-2.69GHz, 3.6GHz-3.7GHz, and 2.39GHz, respectively. Based on these results, it is glaring that designing the MM separately on the Roger RT-6010 and lossy Polyamide substrate materials effectively leads to left-handed characteristics at a lower resonant frequency in comparison to FR4 substrate. This presupposes that the effective property of a MM can be reconstructed by choosing the right substrate material. Table 2 showcases a detailed comparison of resonant frequency for all the substrate materials and their corresponding dielectric constant. On one hand, the resonant frequency increases with decaying dielectric constant. On the other hand, as the MM resonant frequency increases, it exhibits a double negative characteristics arising from the high dielectric permittivity and low loss tangent of the two substrates. Additionally, it is observed that the simulation of the MM using Aluminum Nitride engenders μ_r-negative characteristics at 3.55GHz while both Aluminum Nitride and Polyamide show ϵ_r-negative features at 3.33GHz operating frequency.

In [77], a miniaturized low frequency MM absorber based on a corrugated surface is proposed; however, its 2.5GHz resonance frequency predisposes it to low PTE

and high power dissipation for high power WPT systems. At high MegaHertz and GigaHertz resonant frequency, the magnitude of evanescent waves decays exponentially, leading to power loss and mitigated efficiency. Various coil structures including three coil [14], and four coil structures [57], [58], [60], [78] have been integrated with MM to increase the WPT performance. In [14], [79] a three coil WPT based on insertion of a MM slab is harnessed to optimize the wireless charging efficiency and charging time of mobile phone and laptop applications. The three coil structure in [79] incorporates a planar load MM slab operating at a frequency of 6.78MHz based on AirFuel Alliance Standard [80]. The construction of the MM slab is predicated on a 2 × 3 array of the unit cell, exhibiting a wavelength to length ratio, $\frac{\lambda}{L} = 442.78$ as shown in Fig. 31(a).

At an operating frequency, $f_o = 6.78MHz$, the extracted transmission S-parameter plot, based on HFSS simulation is shown in Fig. 31(b). The planar geometry of the load coil makes it an ideal candidate for consumer electronic applications. Besides, it is worthwhile to state that with the insertion of a MM slab, the measurement result shows a 27% improvement in PTE for the same transfer distance of 50*cm*. In most consumer applications, the transfer power is usually impacted by the presence of ground planes. The complete wireless charging prototype for laptop applications with and without the effect of ground plane considering the
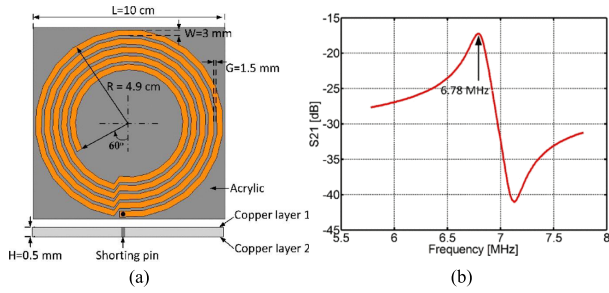
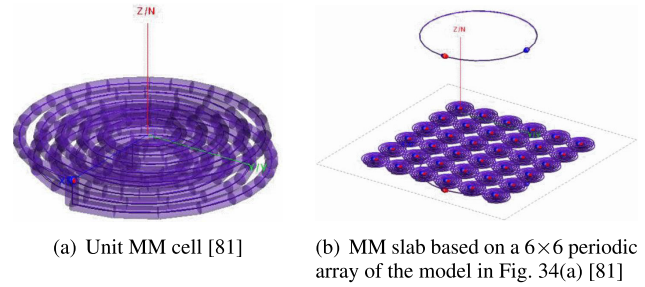**FIGURE 31.** (a) Proposed MM unit cell. (b) Measured S_{21} (in dB) of the MM unit cell. [79].

FIGURE 32. (a) Schematic of a three-coil MM slab for laptop Application (b) Schematic of a 2 × 3 MM-based WPT system with boundary conditions and wave-guide excitation [79].

FIGURE 33. The effect of the load coil position (unit: cm): a) drawn model, b) experimental setup (without ground plane at keyboard for illustration) [79].

MM slab is denoted in Fig. 32 and Fig. 33, respectively. The schematic shows the ground plane situated behind the load coil and separated by a spacing, *S*. By varying the gap, *G*, a comparison analysis of WPT efficiency with and without MMs was investigated with and without a ground plane. For a small value of *G* and assuming no slit on the ground, the lowest value of PTE is observed. This is caused by the divergence/reflection of magnetic flux lines due to the ground plane. However, by increasing the gap to 2*cm*, using the slits as the ground plane while considering the entire transfer distance, an increased value of PTE is recorded. Further, the maximum improvement in WPT efficiency of 55% is observed when the transfer distance is set to 20*cm*. This elicits the practicality of maximizing the PTE, and mitigating the ground impact by increasing the gap. In addition, to evaluate the performance of practical WPT system for laptop application, a laptop model with a keyboard and screen has been designed to assess the impact of angular inclination of the screen relative to the keyboard on the PTE.

(a) Unit MM cell [81]   (b) MM slab based on a 6×6 periodic array of the model in Fig. 34(a) [81]

FIGURE 34. Schematic of a MM slab based on (a) Unit MM cell (b) Periodic 6 × 6 MM slab placed between a transmitter and receiver [81].

Considering 45°, 90° and 135° scenario, it was observed that a 90° angular inclination results in maximum magnetic field coupling with the load coil and hence the highest PTE.

In [81], a miniaturized unit cell MM WPT system based on a three coil structure is proposed. The computer aided design (CAD) of the proposed unit MM cell coupled with the periodically distributed unit cell arrays is shown in Fig. 34(a) and Fig. 34(b), respectively. It is worth noting that the MM design comprises two planar spiral (one right-handed and the other left-handed) connected to create a single resonant inductor. With a thickness of only 1*mm* and resonant frequency of 5.67MHz, the design proves very compact and highly sub-wavelength. Besides, given the same design conditions and parameters, the compact system demonstrates a higher efficiency and impedance values in comparison to a conventional two coil WPT system. The respective efficiency and impedance simulation plots taken with and without the artificial structure are shown in Fig. 35(a) and Fig. 35(b).

As shown in Fig. 35(b), the presence of the MM-slab increases the mutual coupling due to evanescent wave amplification and increased magnetic field coupling between the transmitter coil and receiver coil which in consequence, increases the overall system efficiency as depicted in Fig. 35(a). While the WPT system in the absence of the artificial structure results in a WPT efficiency of 29.8% at a resonance frequency, $f_o = 5.67$MHz, the insertion of the MM between the two loops increases the power transfer efficiency, representing an 8.34% increase in overall WPT efficiency to 39.2%. This increase in system performance based on the inclusion of MM slab is due to the evanescent wave amplification effect of the slab, a phenomenon that engenders a coupling of near magnetic field coupled with a directional channeling of the flux lines towards the receiver coil. Although the design is highly compact compared to current MM structure operating in Gigahertz frequencies, the operating frequency is beyond the handling capacity of existing conventional silicon and MOSFET transistors. Besides, such traditional switches have very low coefficient of resistance which implies a low temperature tolerance. A viable solution is to make use to a wide band gap power semiconductors like Gallium Nitrite (GaN) and Silicion Carbide (SiC). Both semiconductors demonstrate
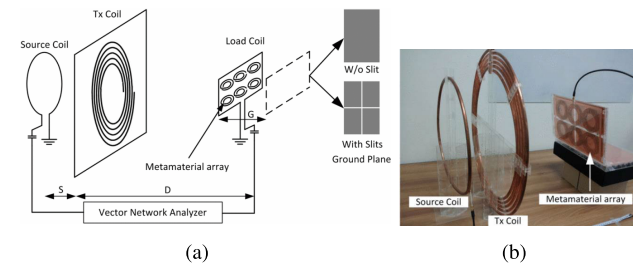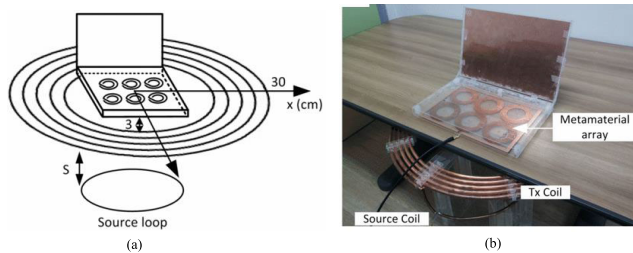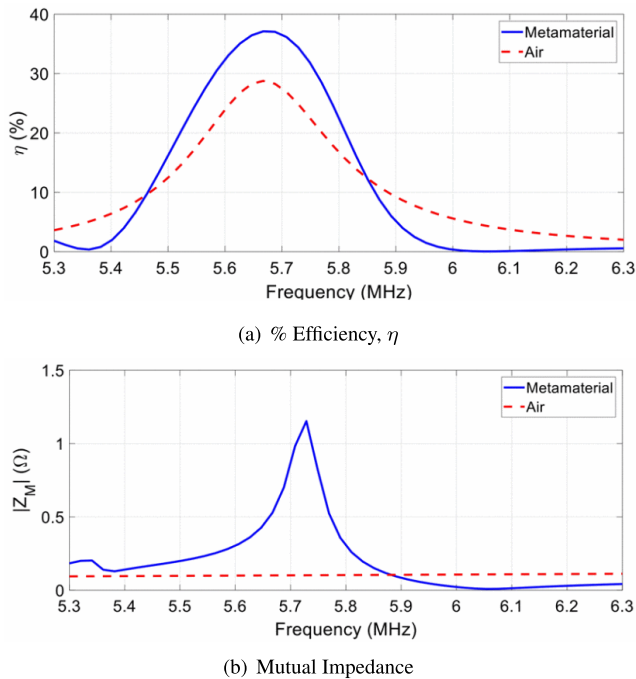
(a) % Efficiency, η

(b) Mutual Impedance

FIGURE 35. Simulation waveforms showing comparison of (a) Efficiency (b) Mutual impedance between the loops before and after insertion of MM-slab.
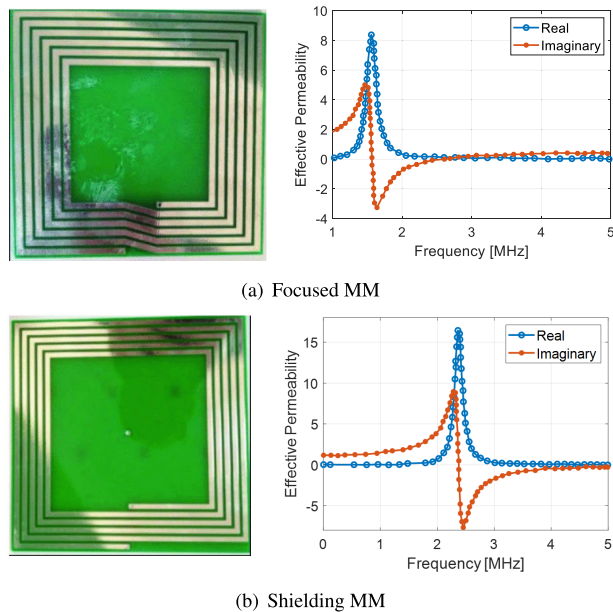

(a) Focused MM

(b) Shielding MM

FIGURE 36. (a) Focused MM and extracted effective permeability (b) Shielding MM and extracted effective permeability [82].

wide energy gap and can operate efficiently under high operating frequencies with minimal losses.

In [82], a four coil WPT model, incorporating a focused MM and shielding MM is presented. The schematic of the amplifying and shielding unit MM cell coupled with the corresponding real effective permeability plots are shown as in Fig. 36(a). Based on the retrieved permeability, the
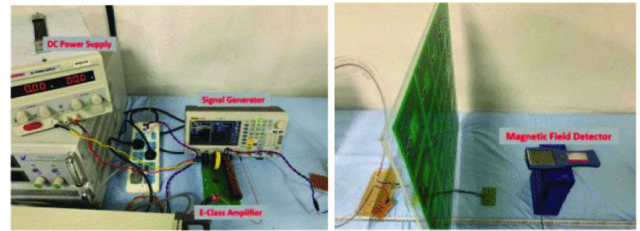
FIGURE 37. Measurement set-up of the four coil MM-based WPT system [82].

TABLE 3. Magnetic field strength of the center and Side of the receiver.

	Magnetic Field strength (A/m) Without Shielding MM	Magnetic Field strength (A/m) With shielding MM
A	0.3803	0.2095
B	0.2492	0.1926

two proposed structures demonstrate negative permeability and near zero permeability characteristics responsible for enhanced PTE and reduced leakage Electromagnetic (EM) field, respectively. The spiral structure is printed on top of the substrate which is also integrated with a lumped capacitor for adjusting the frequency of each unit cell. Both unit cells are identical, the difference being the values of the resonant capacitors. The effective permeability is retrieved based on *S*-parameter method, with both negative permeability and near zero permeability unit cell resonating at a frequency in the 3MHz region. In order to increase the amount of power and improve the PTE, a large surface area MM-slab based on a 4 × 4 array and integration of the two proposed unit cells was harnessed as shown in Fig. 37. The effectiveness of the slab in a WPT system is investigated based on a comparative analysis of the system efficiency and the amount of leakage EMF with and without the MM-slab. With the insertion of the 4 × 4 MM slab, the proposed WPT system achieves a 30% improvement in PTE when the transmission distance is 120*cm*. However, the inclusion of a shielding MM leads to 20mA/m reduction in leakage Electromagnetic field (EMF) is observed. A comparison of the magnetic field of the WPT system with MM and without MM is denoted in Table 3.

The magnetic field of the component incorporating a shielding MM decreases for the two points *A* and *B* under consideration in comparison to the WPT system without shielding. In perspective, the magnetic field decreased from 0.1708*A/m* in A to a value of 0.0566A/m in B. By harnessing a focused MM, the PTE of the WPT system is observed as 30% for a transmission distance of 120*cm*. It is worth noting that the inclusion of shielding MM mitigates the EMF leakage to a value below 0.25*A/m*. 1.6 mm (thickness).

In [59], [84], a high performance hybrid MM slab (HMS) structure based on a systemic arrangement and array of zero permeability and negative permeability unit cell to enhance the performance of a WPT system. It is designed as a dual-layer square structure with a high dielectric constant
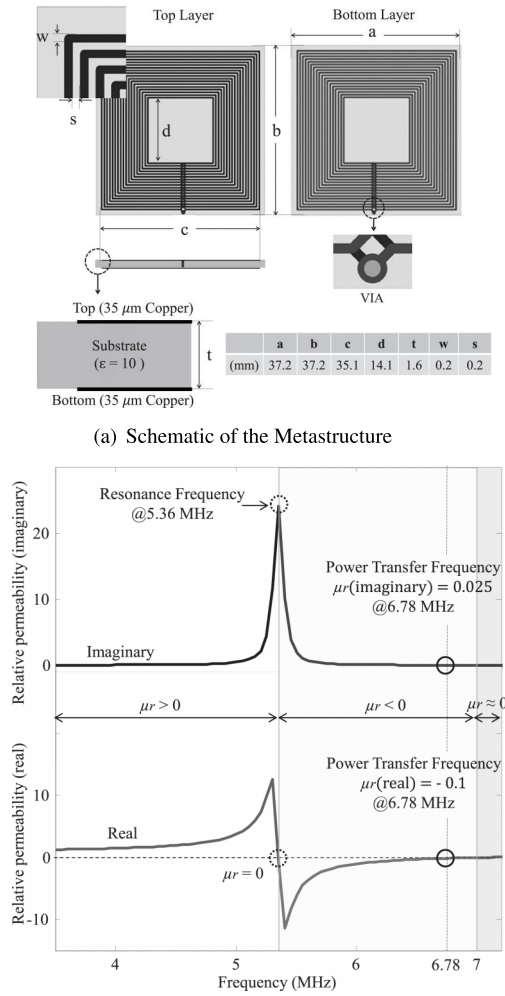
(a) Schematic of the Metastructure

(b) Waveforms of reletive permeability and relative permittivity vs. frequency

FIGURE 38. Relationship between the measured efficiency and (a) Vertical distance, *D* (b) Horizontal distance, D_1 [83].
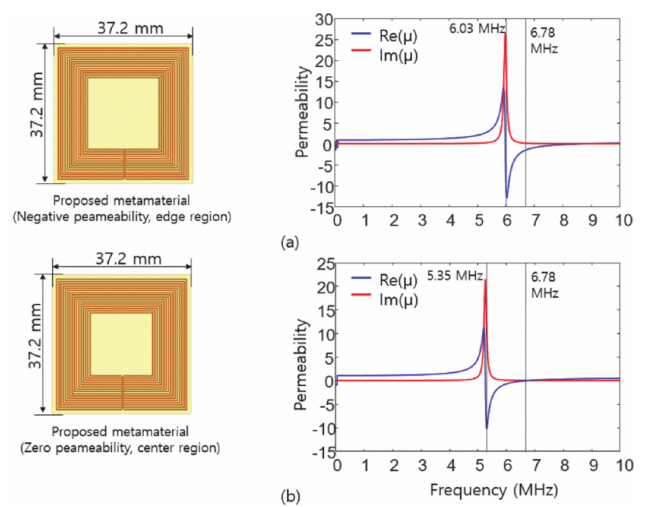

FIGURE 39. (a) Negative permeability metamaterial (b) zero permeability metamaterial [59].

TABLE 4. Parameter Specification for zero and negative permeability MM unit cell.

	Negative Permeability MM unit cell	Zero Permeability MM unit cell
Number of turns	16	18
PCB Substrate	CER-10	CER-10
Number of Layer	2	2
resonant frequency	6.03MHz	5.35MHz
Re(μ)	-1.28	-0.064
Im(μ)	0.0971	0.0154

substrate and fine patterns (0.2 mm). In accordance with Fig. 38(a), the dimension of the unit cell size is 37.2mm (width) × 37.2 mm (length). As shown in Fig. 38(b), the simulated real effective permeability of the unit cell is $\mu_r = -0.1$, characterizing the structure as a MM. In addition, the small value of the imaginary component is indicative of low leakage magnetic flux, and by extension reduced power loss in the system. In perspective, the HMS-based WPT system proposed in [59] enhances the PTE from 35.3% to 41.7% and 10.7% to 18.6% for a distance of 10*cm* and 20*cm*, respectively. Besides, experimental measurement shows a reduction in leakage EMF from -12.21*mT* to -26.03*mT* for a 6.78MHz WPT system. A more efficient topology based on two starked HMS structure is introduced in [85] for enhanced performance. When the MM structure is placed between a *Tx* and *Rx*, the PTE increased from 23.9% to 49.3% and 6.9% to 29.4% for a *Tx* to *Rx* separation of 15*cm* and 20*cm*, respectively. While this study demonstrates a significant progress in increasing the penetration of

MM-based WPT, it does not provide sufficient measurements and experimental results for performance validation.

The fundamental structures of an hybrid MM slab proposed in [59], comprising a negative and positive permeability unit cell and their corresponding effective permeability waveforms are depicted in Fig. 39(a) and Fig. 39(b), respectively.

As shown in Table 4, both structures are fabricated with 18 turns and 16 turns of wire, respectively. In addition, a cascade layer of each structure is separately designed on a CER-10 PCB substrate. On one hand, it is note-worthy that by exploiting the electromagnetic boundary conditions, the negative permeability unit MM changes the propagation direction of the diverging magnetic flux emanating from the transmitter and focuses the amplified magnetic field towards the receiver while also mitigating the leakage of magnetic flux. On the other hand, the zero permeability material contributes to the enhancement in transfer power and efficiency by channeling the magnetic flux in a straight path towards the receiver. As seen in Fig. 39, the full-wave EM-simulation result shows both the zero and negative μ_r structures demonstrate a resonant frequency (f_{res}) and real permeability, $\Re(\mu_f)$ corresponding to (-1.28, 5.35MHz), and (-0.064, 6.03MHz), respectively. By changing the number of turns, the MM can effectively adjust the resonance operating frequency.
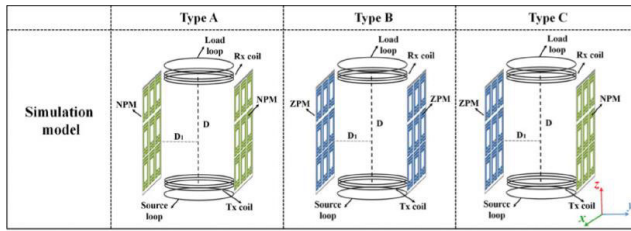
FIGURE 40. Three system simulation models of the side-placed NPM slabs, ZPM slabs, and combination of the NPM and ZPM slabs [83].
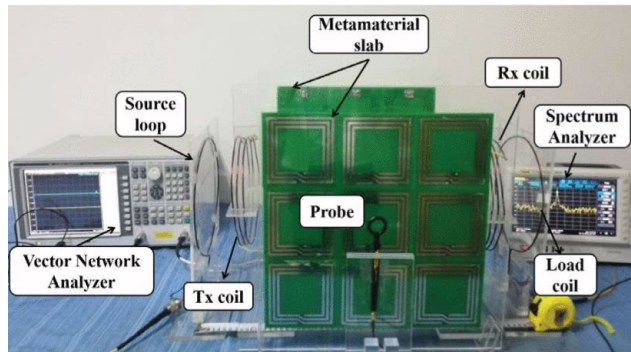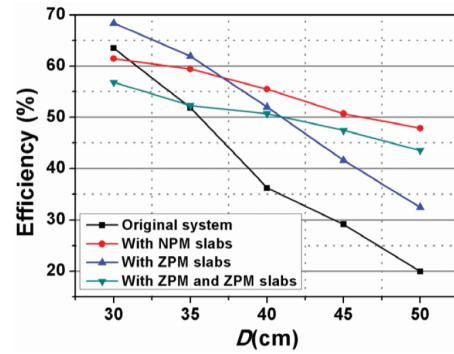

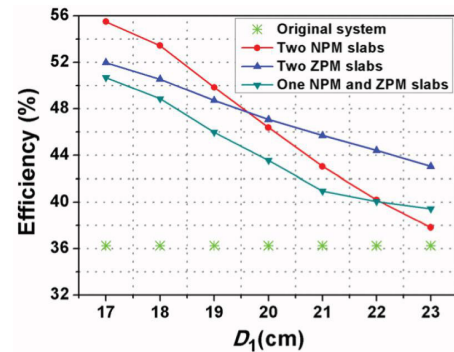**FIGURE 41.** Experimental test-bed of the side-placed MM WPT structure [83].

(a) Efficiency vs.vertical distance, D

(b) Efficiency vs.horizontal distance, D_1

FIGURE 42. Relationship between the measured efficiency and (a) Vertical distance, *D* (b) Horizontal distance, D_1 [83].

The study in [83] presents a comprehensive investigation of the impact of two sided MM design in a WPT system. Based on a four coil structure (comprising the source coil, transmitting coil, receiving coil and loop coil), three disparate models of the two side-placed MMs including zero permeability MM (ZPM), negative permeability MM (NPM), and a melange of ZPM and NPM were separately simulated to determine the topology with optimal WPT efficiency and minimum leakage EMF.

In line with Fig. 40, and considering the distances, $D_1 = 17cm$ and $D = 40cm$, representing the horizontal displacement from the central axis and vertical spacing between the Tx and Rx coil, respectively; the simulation results show an enhancement in magnetic field distribution for the three considered topologies. However, it is observed that the field distribution behind the NPM slab increases for the simulated results in comparison to the measured results. Moreover, a reduction in the field strength outside the ZPM slab is observed coupled with an increase in the magnetic field around the Rx coil. Furher, based on the experimental set up in Fig. 41, measurements of the transmission efficiency were taken for a fixed distance, $D = 30cm$.

The VNA-AV-3656A vector network analyzer was harnessed to supply signal to the Tx coil and the transmission scattering parameter, S_{21}, was measured after the standard two-port calibration while both the spectrum analyzer (RS03030-TG) and probe were exploited for magnetic field measurement. Taking the resistance of the Tx and Rx coils as 50Ω and varying the distance from source to Tx and load to Rx to achieve impedance matching, the system efficiency,

η is evaluated based on the scattering parameters of the transmission and reflection as shown in Equation (50)

$$\eta = |S_{21}|^2 \times 100\% \qquad (50)$$

The PTE and leakage EMF of the original system without MM was first measured and afterward compared with PTE and leakage EMF of the other side-placed MM-based WPT topologies. Fig. 42(a) and Fig. 42(b) shows the variation of WPT efficiency with vertical distance (D) and horizontal distance D_1, respectively for different combinations of side-placed MM. For the NPM slab, it was observed that the smallest PTE corresponds to a short transfer distance while higher values of PTE are observed as the transfer distance increases. This finds explanation in the inherently high power loss of the NPM slab at short transfer distance. In addition, this behavior can also be attributed to efficiency splitting due to resonant frequency deviation. Moreover, the efficiency value based on combining the ZPM and NPM slab is lower than that of two NPM slabs as D increases whereas a combination of NPM and ZPM slabs generates much higher than that of ZPM slabs as D exceeds $40cm$. This is due to the attenuating effect of the magnetic field reflected by the ZPM slab over large transfer distance which lowers the amount of magnetic field that reaches the receiver. The influence of magneto-inductive wave/ evanescent wave amplification (an intrinsic property of NPM slab) is responsible for PTE enhancement inspite of the increase in transfer distance.

C. METAMATERIAL BASED WPT FOR MISALIGNMENT COMPENSATION

Misalignment between a transmitter (*Tx*) and receiver (*Rx*) coils is a critical factor largely responsible for performance deterioration in WPT systems. It is basically a consequence of phase mismatch between *Tx* and *Rx*, which eventually culminates in a divergence of flux lines and power loss as the distance between the *Tx* and *Rx* coil increases. In order to achieve efficient wireless transfer, a perfect coupling of the coil structures is a key requirement. Notice that when a WPT system is subjected to lateral or angular misalignment from its initial position, a cross coupling between the coils ensues, leading to depreciation in overall performance [86]. In a bid to mitigate the impact of misalignment on WPT performance, ample research has been linked to PTE degradation and a drop in power transfer to misalignment between *Tx* and *Rx* coils [63], [73], [87]. The impact of lateral misalignment on WPT performance is discussed in [87]. For a transfer distance of $d_l = 100cm$ and considering a purely aligned WPT scenario with MM slab incorporated, the PTE increased from 25.3% to 57.9%. Under lateral misalignment condition, the PTE of the WPT system with MM slab improves by 33.1% and 27.3% corresponding to lateral misalignments, $D_L = 10cm$ and $40cm$, respectively. However, in the case of angular misalignment, θ, and for the same transfer distance, d_l, and a resonant operating frequency, $f_o = 6.6MHz$, it has been reported that the PTE improved by 32.9% and 30.9% for $\theta_1 = 15^o$ and $\theta_2 = 45^o$, respectively. This further accentuates the effectiveness of the MM slab in optimizing WPT performance under misalignment situation.

Using the same methodology proposed in [63], Chen and Tan [63], exploited a single 2×2 array of MM unit placed between the *Tx* and *Rx* coils to investigate the performance enhancing ability of MM under severe lateral and angular misalignment scenarios. Experimental measurement shows an improvement in PTE from 7.8% to 45.8% for a coil spacing of $30cm$ and a lateral misalignment, $D_L = 6cm$ while the PTE is increased to 35.3% and 31% for the coil's angular displacement, $\theta = 30^o$ and $\theta = 45^o$, respectively. While the MM slab has demonstrated its capability for WPT performance enhancement, the low value of the efficiency is indicative of high system loss and brings up the need for infuse optimality into the system operation. Thus, it is apparent that by leveraging the magneto-inductive wave amplification property of MM through its incorporation WPT system, it can effectively mitigate the impacts of misalignment on the PTE and power transfer in a WPT system while offering practical solutions ways for electronic charging devices with increased misalignment tolerance. In [83], analysis and performance comparison of angular and lateral misalignment of side-placed negative permeability MM (NPM), zero permeability MM (ZPM) and a melange of NPM-ZPM side-placed MM structures are investigated. The diagrammatic depiction of the lateral and angular misalignment scenarios is shown in Fig. 43(a) and Fig. 43(b), respectively. In the case of lateral misalignment, the receiver is offset along the y-axis
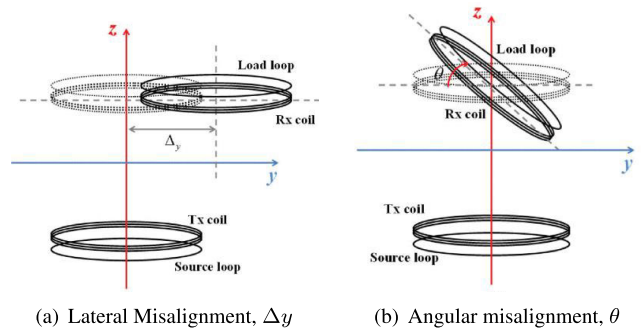

(a) Lateral Misalignment, Δy (b) Angular misalignment, θ

FIGURE 43. Schematic of the WPT system showing offset of the receiving coil (Rx) (a) lateral misalignment, Δy (b) angular misalignment, θ.
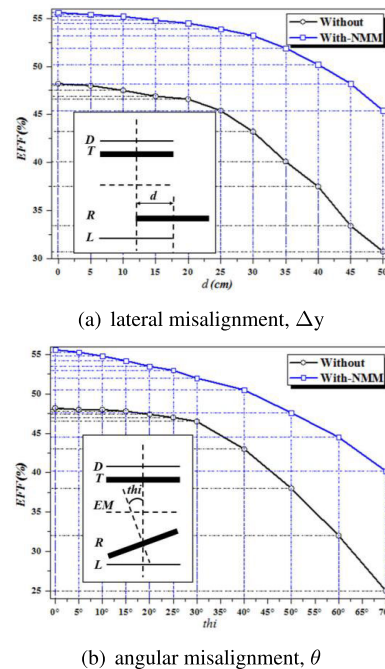

(a) lateral misalignment, Δy

(b) angular misalignment, θ

FIGURE 44. Measurement efficiency of the WPT system with various misalignment. (a) lateral misalignment, Δy. (b) angular misalignment, θ [83].

while a displacement of the receiver at an angle θ around the x-axis represents the angular misalignment. In view of the movable range limitation imposed on *Rx*-coil, the vertical distance, $D = 50cm$ is considered for misalignment of the receiving coil while lateral misalignment is varied from 0 to $14cm$ for a step size of $2cm$.

Fig. 44(a) and Fig. 44(b) show a comparison of efficiency for various lateral misalignment and angular misalignment, respectively. Based on set-up, the PTE of the actual system at D = 50cm without lateral misalignment of the coil is obtained as 19.98%. Nonetheless, incorporating the two side placed NPM or ZPM slabs increased the PTE to 47.98% (32.49% improvement) for lateral misalignment, $\Delta y = 0$ and D = 50cm whereas to PTE increased to 43.56% when the combination of NPM and ZPM slabs is applied. In general, the WPT efficiency decreases as θ increases. However, with the insertion of MM slabs, the efficiency is substantially enhanced compared to the actual system under angular

misalignment conditions. From Fig. 44(b), it is apparent that at $\theta = 60^o$, the efficiency of the system with MM slab is higher than that of the actual system with $\theta = 0$. In the same vein, at $\theta = 45^o$, the system efficiency for the ZPM slab model and a combination of ZPM and NPM slab is higher than the PTE of the actual system, whereas at $\theta = 90^o$, both the actual WPT system and side-placed MM topologies post nearly zero PTE due to weak coupling between the coils.

In [16], a compact MM-based fully planar MRC-coupled WPT is designed to improve the efficiency of WPT systems. Using a MM slab based on a 3×3 array of the MM unit structure, an improved efficiency of 18% is observed compared to the system without MM loading. However, the occurrence of transmission and reflection of magnetic field are delayed owing to the GHz resonant frequency of the MM structure. In [88], the effect of electromagnetic MM on the performance of mid range WPT systems under lateral and angular misalignment is rigorously investigated. The manuscript presents strategies for enhancing the stability of medium range wireless designs and improving misalignment tolerances of WPT systems. Based on the experimental design, it is observed that the transfer efficiency was maintained at 45% when the distance of the MM-slab with respect to the receiver is $1000mm$ and the resonant coil is laterally misaligned by about one coil diameter. Further, considering an angular displacement of 70°, it is observed that the system maintained a stable transfer efficiency more than 40%. However, neglecting the effect of MM and keeping the operating conditions constant, the observed efficiency drops to 30% and 25% for lateral misalignment and angular misalignment, respectively.

D. MM-BASED WPT DESIGN FOR CONSUMER APPLICATIONS

Various coil structures including three coil [14], [79], four coil structures [57], [58], [60], [78] have been integrated with MM to increase the performance of a WPT system. In [14], [79] a miniaturized unit cell MM having a wavelength to length ratio, $\frac{\lambda}{L} = 170$ *and* 442.78, respectively) based on three coil structure. Fig. 32(a) is adopted for powering mobile application. The uniqueness of this design stems from a consideration for the impact of ground effect on the WPT efficiency. The design is based on a three coil structure made of a planar load coil and operates at a resonant frequency of 6.78MHz based on Air-Fuel Alliance Standard. The planar geometry of the load coil makes it adaptable for consumer electronic applications. The WPT schematic showing the ground plane is denoted in Fig. 32(a). The equivelent prototype MM design for measurement analysis is depicted Fig. 32(b). Based on Fig. 32(a), the ground plane is situated behind the load coil separated by an air gap, S. By varying the gap, G, a comparison analysis of WPT efficiency with and without MMs was investigated. It is observed that harnessing a small value of gap, G and neglecting the effects of ground plane results in the lowest value of PTE. In addition, without taking the ground plane

into consideration, a maximum efficiency improvement of 27% is observed with MMs compared to without MMs. This low PTE value has been attributed to the divergence/reflection of magnetic flux lines due to the absence of the ground plane. However, by increasing the gap to $2cm$, and using the slits as the ground plane while considering the entire transfer distance, an increased value of PTE is recorded coupled with a maximum improvement in WPT efficiency of 55% when the transfer distance is set to $20cm$. This elicits the possibility of maximizing the PTE, and mitigating the ground impact by increasing the gap. In order to evaluate the performance of practical WPT system for laptop application, a laptop model with a keyboard and screen has been designed to assess the impact of angular inclination of the screen relative to the keyboard on the PTE. Considering 45°, 90° and 135° scenario, it was observed that 90° displacement angle results in maximum magnetic field coupling with the load coil and hence the highest PTE. Neglecting the effects of ground plane, and using a transfer distance, $D = 35cm$, a maximum efficiency improvement of 27% is observed when the MM is placed $2cm$ in front of the load coil. In addition, to evaluate the performance of practical WPT system for laptop application, a laptop model with a keyboard and screen has been designed to assess the impact of angular inclination of the laptop screen relative to the keyboard on the PTE. Considering 45°, 90° and 135° scenario, measurement shows the 90° results in maximum magnetic field coupling with the load coil and hence the highest PTE.

E. CONDUCTIVE METAMATERIAL(MM) DESIGN BASED ON 3D PRINTED TECHNOLOGIES

Over the past few decades, various methods had been adopted to enhance and accelerate the processing and prototyping of MM-based WPT models. It is worth noting that of paramount importance to realizing enhanced performance is the adoption of efficient fabrication strategies that allow for a conduction of electric current while achieving improved system performance with minimal material consumption. As a consequence of advances in fabrication technologies, various kinds of conductive materials, including 3D printed electronics have brought new modality to 3D-printed designs, with enhanced capability for depositing conductive materials on the 3D substrate using aerodynamic focusing technique [89]. Meanwhile, various other method currently adopted for construction of conductive connections and traces within a 3D structure is provided in Mahto and Sniderman, ElectroJet from ChemCubed [90], being a case in point. Another notable example is the Nano dimension DragonFlyTMPro [91] combining a multi-material inkjet printing and nano-ink technology to build 3m thick layers with two materials (one nano-silver ink, one dielectric polymer ink). A critical performance enabler in a 3D-printed electronic or MM is the conductive ink. A high performance conductive ink or paste is very vital to realizing a conductive trace and by extension an a high efficiency WPT system. This brings up the potential of material property such as
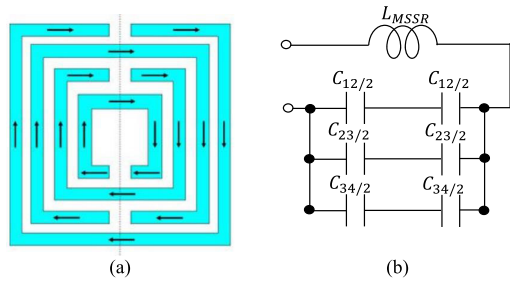
FIGURE 45. (a) MSRR with split-rings. (b) Quasi-static equivalent circuit of the MSRR reported in Fig. 45(a) [97].
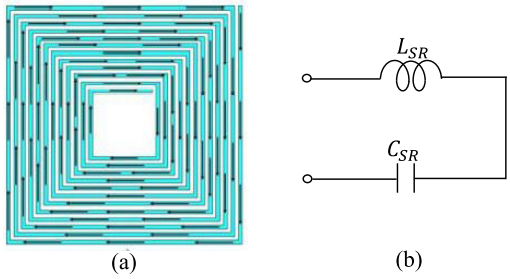

FIGURE 46. (a) SR with turns. (b) quasi-static equivalent circuit of the SR shown in Fig. 46(a).

conductivity and oxidative strength as having a significant influence on the effectiveness and suitability of a 3D printer. To this end, Nano-silver ink, which is one of the most popular 3D printing inks has been widely used in 3D printing of electronics on substrate. While it is silver inks are preferred to aluminum/copper/silver wires because of their high conductivity and oxidative stability [92], the inherently high resistivity of silver ink limits its application in WPT system as compared to using copper/silver wires. For instance, the volume resistivity (the reciprocal of conductivity) of the silver ink provided by Voxel8 is $3 \times 10^{-8}\Omega m$ [93], approximately 17 times more than that of the pure copper. Therefore in some applications, post-processing techniques were introduced after the cold extrusion/printing for better electrical/electromagnetic performance, including annealing [94], hot-pressure sintering [95] and laser sintering [96].

VI. NUMERICAL MODEL AND EQUIVALENT CIRCUIT REPRESENTATION OF MM BASED WPT

In [97], the design and analysis of a miniaturized resonant inclusions for practical realization of MM samples with anomalous values of the real part of the permeability is presented. For comparative analysis, the study considered various inclusions, including multiple split-ring resonators (MSRRs), which is a straightforward extension of the commonly used split-ring resonators (SRRs), and the spiral resonators (SRs), that enable a greater miniaturization rate. The physical impact and influence on the resonance mechanism, system performance and inherent saturation of the resonant frequency when increasing the number of rings of the MSRRs and the number of the turns of the SRs are given in the paper. The schematics of the

MSSR and SRR and their equivalent circuit representations are denoted in Fig. 45 and Fig. 46, respectively. The proposed structure is similar to the one analyzed in [54] but slightly different from the one proposed in [98], [99]. While the analytical models investigated in [54], [98], [99] are imperative to understanding the physical phenomena influencing the behavior of SR, they either suffer from inaccurate design formulas or are limited to a given number of turns. In perspective, the model proposed in [98], [99] is only applicable for number of turns, $N = 2, 3$ whilst the one in [54] is an approximate model, only relevant for a preliminary rough design of the inclusion. The above drawbacks serves as a motivation for investigating a new and accurate analytical design formulas, based on a the proposed quasi-static model in [97]. Both MSRRs and SRs were derived and tested while also comparing the generated result with the formula-based solutions and full-wave numerical results. It is worthwhile to know that due to the μ-negative property of MSRRs and SRs and the inherent miniaturization of both trans-missive and radiating components, they have proven a very efficient alternative in reducing the electrical dimensions of the resonant inclusions when synthesizing artificial MM. The above discovery was based on a derivation of new and accurate analytical designs and quasi-static model, for both MSRRs and SRs followed by testing through a comparison with existing formulas and full-wave electromagnetic simulations. The new proposed model shows improved accuracy while also controlling the interaction of the electromagnetic field with the MSRR and SR. While the MSSR achieves miniaturized linear dimensions in the order of $\frac{\lambda_o}{30}$ -$\frac{\lambda_o}{40}$ (λ_o is the medium electromagnetic wavelength), the utilization of SRR inclusion can increase the chances of realizing a more miniaturized electrical dimensions in the range of $\frac{\lambda_o}{65}$ - $\frac{\lambda_o}{250}$, using printed circuit technologies. Further, the adoption of high permeability substrate and high-precision lithographic process can culminate in a compact electrical dimensions of the MSRR and SR can be realized by backing the inclusions with a high-permittivity substrate as well as using more expensive high-precision lithographic processes capable of beating the limit of $0.1mm$ for conventional technologies. The inductance of the MSRR was derived using inductance of the expression from one of the circular (or squared) loop having an equivalent radius (or side) given by the average between the inner and the outer radii (or sides) of the rings [13]–[15].

$$L_{MSRR} = \frac{\mu_o}{2} \frac{l_{avg}^{MSRR}}{4} \times 4.86 \, ln\Big[\frac{0.96}{\rho} + 1.86\rho\Big] \quad (51)$$

where l_{avg} is the average strip length calculated over all the N rings as

$$l_{avg}^{MSRR} = \frac{1}{N}\sum_{n=1}^{N} l_n = 4(l - (N-1)(s+w)) \quad (52)$$

Besides, accurate determination of the inductance entails giving consideration to how the multiple rings fill the
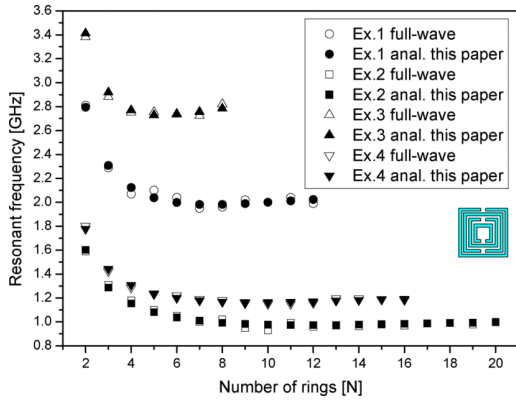
FIGURE 47. (a) Plot of resonant frequency of MSRR against number (N) of turns, showing comparison between full-wave simulations and analytical results for different MSRRs, whose geometrical data are the same as in the caption of Fig. 45.

available area. This effect was captured by considering the fill effect based on the fill factor, ρ as depicted in:

$$\rho = \frac{l - l_N}{l + l_N} = \frac{(N-1)(w+s)}{l - (N-1)(w+s)} \quad (53)$$

where s, l, w are the dimensions of the MSRR structure. Similarly, the overall capacitance of the MSRR structure is modeled as shown in (54)

$$C_{MSRR} = \frac{N-1}{2}[2l - (2N - (N-1)(s+w))]C_o \quad (54)$$

where

$$C_o = \epsilon_o \frac{K(\sqrt{1-k_o})}{K(k)}; \quad k = \frac{s/2}{w + s/2} \quad (55)$$

In the same vein, the distributed capacitance between adjacent turns of the *SRR* structure was derived as presented below.

$$C_{SR} = C_o \frac{l}{4(w+s)} \frac{N^2}{N^2+1} \sum_{n=1}^{N-1} \left[l - (n + \frac{1}{2})(w+s) \right] \quad (56)$$

Note that C_{SR} vanishes in the case of a single turn, $N = 1$. However, when N increases beyond a certain threshold, it is expected that the contribution of the distributed capacitance associated to the inner turns becomes progressively less significant, leading to a saturation in C_{SR}. The total inductance of the *SR* can be modeled by considering a very simple formula for the self-inductance of a single turn with an average total length given as (57)

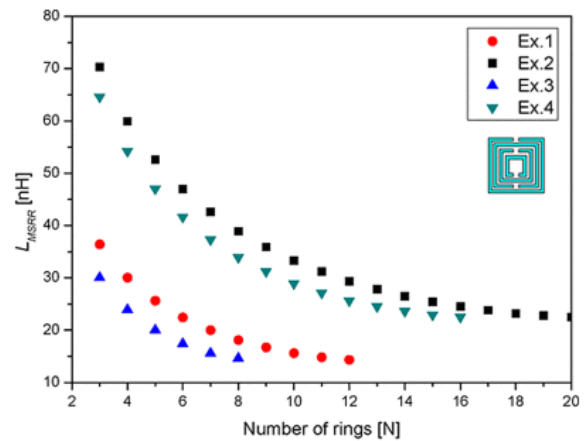$$L_{SR} = \frac{\mu_o}{2\pi} l_{avg}^{SR} \left[\frac{1}{2} + ln(\frac{l_{avg}^{SR}}{2w}) \right] \quad (57)$$

where:

$$l_{avg}^{SR} = \frac{1}{N} \sum_{n=1}^{N} l_n = \frac{4lN - [2N(N+1) - 3](s+w)}{N} \quad (58)$$

The resonant frequency plot, a factor of the compactness of the system against the number of rings is shown in Fig. 47. The waveform indicates a reduction in frequency as the number of turns increases. Moreover, the figure shows
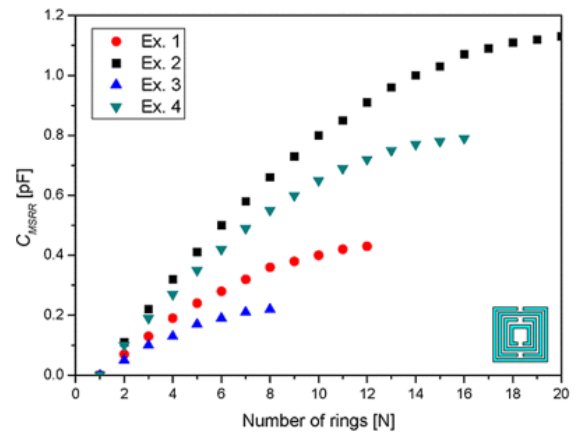
(a)

(b)

FIGURE 48. (a) Total Capacitance and (b) total inductance as a function of the number of turns of the MSSR reported in Fig. 45 with comparison among different models and geometrical parameter.

a comparative analysis of the quasi-static model and full wave simulation based on the models proposed in [54], [98], [99]. In order to validate the proposed circuit model of the MSRR, some comparisons with full-wave numerical simulations have been performed. The agreement between the quasi-static model and the simulated result is very good, as confirmed by the examples reported in Fig. 48. From a practical standpoint, when the number of the rings increases to a certain threshold, there does not exist a further reduction of the resonant frequency and as such assumes a constant value. As earlier explained, in fact, the increasing rate of the total distributed capacitance reduces when increasing the number of the rings, while the decreasing rate of the total inductance decreases, as well. The final combined effect is that the resonant frequency of the MSRR can be reduced appreciably up to 3–4–5 rings (it depends on the fill ratio, ρ of the MSRR depicted in (57), while the fine-tuning of the resonant frequency can be achieved by varying the number of rings. However, after a certain threshold, the resonant frequency is stabilized, essentially making the introduction of further rings of non-effect in reducing the resonant
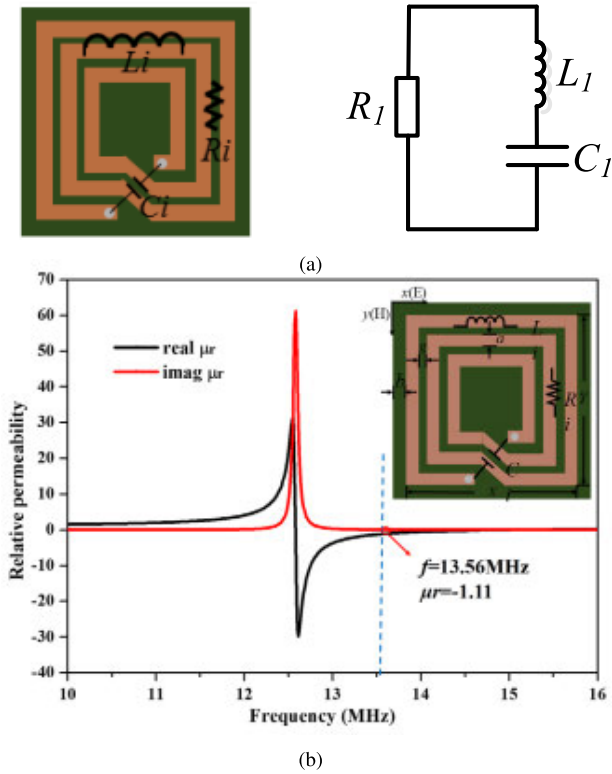
(a)

(b)

FIGURE 49. (a) Left- schematic of the unit MM cell. Right - RLC lump circuit equivalence of the unit MM cell (b) Effective permeability of the unit cell.

frequency. Additionally, when the fill ratio approaches 1, the decreasing ratio of the inductance is greater than the increasing ratio of the capacitance and a slight increase of the resonant frequency is observed. In [53], an analysis and equivalent circuit model of a MM using simple qualitative and quantitative explanation for the behavior of MM in WPT is presented. A full wave EM simulation of MM-based WPT system is carried out using ANSYS HFSS simulator. The proposed circuit structure of the MM fed WPT system was subjected to numerical calculation while comparing the design characteristics with results based on advanced system design simulation. The 3D-schematic of the proposed unit cell/equivalent lumped circuit representation coupled with the associated effective permeability waveform are illustrated in Fig. 49(a) and Fig. 49(b), respectively. Note that R_1, L_1 and C_1 are the parasitic resistance, parasitic capacitance and parasitic inductance of the unit cell, respectively. The effective permeability curve shows the unit cell resonates at a frequency ≈ 13.56MHz.

In order to increase the density of magnetic flux while mitigating the leakage electromagnetic waves and increasing the transmit power, a MM-slab based on a 3×3 array of the unit cell is proposed in [53]. The simulation of the MM slab in ANSYS high frequency structured simulator (HFSS) and Keysight advanced design system (ADS) is presented in Fig. 50. In addition, Fig. 51(a) indicates the magnetic field magnitude and distribution when the MM is placed in the middle of the WPT system. In addition, Fig. 51(b) indicates
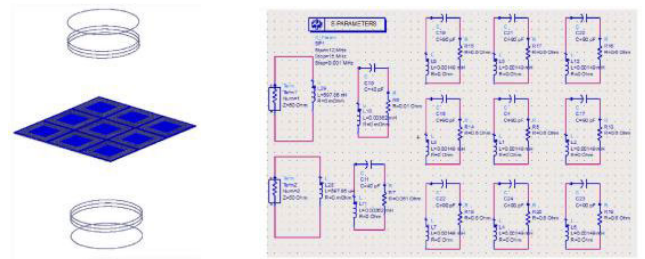

FIGURE 50. (LEFT) Circuit schematic of the four coil MM-WPT as modeled in ANSYS HFSS. (RIGHT) The equivalent RLC resonance circuit of the MM-WPT structure as modeled in Keysight ADS.

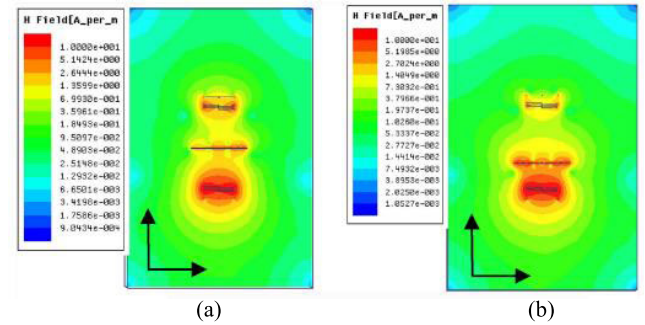(a)   (b)

FIGURE 51. Comparison of the magnetic field distribution of WPT system based on MM placed (a) In the middle of system (b) Far from the transmitter of 150*mm*.

the distribution of magnetic field considering a transmitter to MM-slab distance of 150*mm*. While the magnetic field intensity between the transmitter and receiver decreases as the transmitter to MM distance increases, it is observed that placing the MM in the middle of the coils results in higher magnetic field intensity as compared to when it is near the transmitter.

Going forward, the transmission scattering parameters, S_{21}, which represents the efficiency of the system is obtained by varying the position of the MM-slab relative to the exciting coils while taking measurement values at each position. The simulation plot of S_{21} magnitude against frequency under varying transfer distance is shown in Fig. 52. When the transfer distance is fixed at 200*mm*, and the distance between the MM and transmitting coil is varied from 100*mm* to 250*mm*, the resonance frequency is observed to vary between 12MHz-15MHz while the frequency corresponding to the maximum S_{21} is ≈ 13.56 MHz. Admittedly, the value S_{21} is closely related to the loading position of MM. In line with Fig. 52, it is observed that when the MM is located away from the transmitting coil, the values of S_{21} first increase and then decrease, corresponding to S_{21} peaks ranging from 40% to 50%. It is also worth stating that the amplitude of S_{21} attains its maximum when the MM is placed in the middle of the WPT system, indicating the possibility of achieving a better transmission efficiency by placing the MM in the middle. Consistent with [100], [101], the numerical evaluation of S_{21} is obtained based on [78].

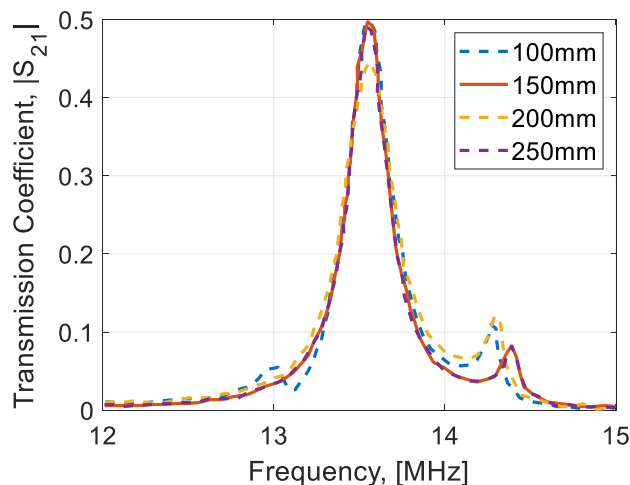$$S_{21} = 2 \frac{V_L}{V_s} \sqrt{\frac{R_s}{R_l}} \qquad (59)$$

FIGURE 52. Comparison of the S_{21} magnitudes when the location of metamaterial (MM) varies.
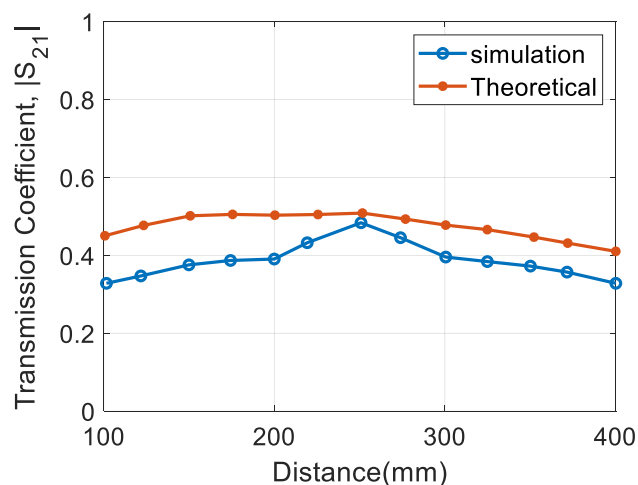

FIGURE 53. Comparison of the simulation and calculation of the S_{21} when the location of MA varies.

where V_L, V_S, R_S, and R_L are the load voltage, source voltage, source resistance, and load resistance, respectively. Moreover, a comparative analysis of transmission scattering parameter, S_{21} based on ADS simulation and numerical calculation using equivalent circuit analysis is presented in Fig. 53. As exhibited in Fig. 53, it is obtrusive that variations in the location of 3 × 3 MM-slab lead to a corresponding change in value of S_{21}. Besides, a slight increase in the simulation compared to calculation results is observed for all the simulation parametric distances; nevertheless, the values from both cases closely match, effectively validating the accuracy of the equivalent circuit model in verifying the transfer characteristics of the MM-based WPT system.

VII. CONCLUSION

This paper has presented an in-depth review and critique of different MM-based WPT structure based on operating resonant frequency range, fabrication process and three dimensional (3-D) technologies. In addition, the methodolo-

gies involved in the full wave electromagnetic simulation of the MM models are based on ANSYS HFSS electromagnetic solver and ADS. ANSYS is useful for extracting material parameters, including the transmission scattering parameter (S_{12} and S_{21}), reflection scattering parameter (S_{11} and S_{22}), effective permeability (μ_r) and effective permittivity ϵ_r). The effects on μ_r and μ_r in ascertaining the existence of left handed characteristic have been broadly expounded. Based on literature account, the resonant frequency where evanescent coupling of near magnetic field occurs for high power application was discovered to be very low compared with those other RF and microwave MM structures. Of very paramount note is the deteriorating effect of high resonant frequency on evanescent wave amplification coupled with the increased magnitude of leakage inductance arising from most commonly existing MM design. Design parameter optimization criterion has been formulated to understand the impact of tuning key design parameters on the resonant operating frequency. Essentially, fabricating a low frequency MM entails increasing the number of turns and minimizing the inter-turn distance given that the parasitic inductance and capacitance of MM which hiolistically constitute the *LC* resonant frequency depends on the number of turns and spacing between adjacent turns. While the optimized resonant frequency of the structure in some of the reviewed papers are very small in comparison to the RF and microwave frequencies of existing MM, it is still considered very high, especially for high power applications utilizing semiconductors. At high operating frequency, the switching transitions of semiconductors increases significantly, leading to increased dead time, switching stress and performance degradation. In light of this, future work should focus on further reducing the resonant frequency to 85kHz. Further, for practical realization of MM-based WPT system, a critical area that is worth investigating is the optimal placement of an MM slab. Even though different slab positions have been harnessed in literature, including slab placement between the transmitter and receiver, it is apparent that such location puts the slab in the power transmission path, essentially deteriorating the practicality of WPT systems. While an ideal position could be to attach the slab to the coil surface, such an approach will distort the concentration and convergence of magnetic flux, leading to flux leakage, power dissipation, and a dimunition of power transfer efficiency.

REFERENCES

[1] N. Tesla, "Apparatus for transmitting electrical energy," U.S. Patent 1 119 732, Dec. 1, 1914.

[2] N. Tesla, "High frequency oscillators for electro-therapeutic and other purposes," *Proc. IEEE*, vol. 87, no. 7, p. 1282, Jul. 1999.

[3] F. Zhang, X. Liu, S. A. Hackworth, R. J. Sclabassi, and M. Sun, "*In vitro* and *in vivo* studies on wireless powering of medical sensors and implantable devices," in *Proc. IEEE/NIH Life Sci. Syst. Appl. Workshop*, Apr. 2009, pp. 84–87.

[4] N. M. Neihart and R. R. Harrison, "Micropower circuits for bidirectional wireless telemetry in neural recording applications," *IEEE Trans. Biomed. Eng.*, vol. 52, no. 11, pp. 1950–1959, Nov. 2005.

[5] R. Narayanamoorthi, "Modeling of capacitive resonant wireless power and data transfer to deep biomedical implants," *IEEE Trans. Compon., Packag., Manuf. Technol.*, vol. 9, no. 7, pp. 1253–1263, Jul. 2019.

[6] G. Wang, W. Liu, M. Sivaprakasam, and G. A. Kendir, "Design and analysis of an adaptive transcutaneous power telemetry for biomedical implants," *IEEE Trans. Circuits Syst. I, Reg. Papers*, vol. 52, no. 10, pp. 2109–2117, Oct. 2005.

[7] A. K. R. Rakhyani, S. Mirabbasi, and M. Chiao, "Design and optimization of resonance-based efficient wireless power delivery systems for biomedical implants," *IEEE Trans. Biomed. Circuits Syst.*, vol. 5, no. 1, pp. 48–63, Feb. 2011.

[8] J. Park, S. H. Kim, and O. Jeong, "Use case and service framework for WPT (wireless power transfer)," in *Proc. 16th Int. Conf. Adv. Commun. Technol.*, Feb. 2014, pp. 1027–1030.

[9] A. Kurs, A. Karalis, R. Moffatt, J. D. Joannopoulos, P. Fisher, and M. Soljačić, "Wireless power transfer via strongly coupled magnetic resonances," *Science*, vol. 317, no. 5834, pp. 83–86, Jul. 2007.

[10] (2018). ORNL. *ORNL Demonstrates 120-kilowatt Wireless Charging for Vehicles*. Accessed: Mar. 25, 2019. [Online]. Available: https://www.ornl.gov/news/ornl-demonstrates-120-kilowatt-wireless-charging-vehicles

[11] E. Waffenschmidt and T. Staring, "Limitation of inductive power transfer for consumer applications," in *Proc. 13th Eur. Conf. Power Electron. Appl.*, Sep. 2009, pp. 1–10.

[12] K. Knaisch, M. Springmann, and P. Gratzfeld, "Comparison of coil topologies for inductive power transfer under the influence of ferrite and aluminum," in *Proc. 11th Int. Conf. Ecol. Vehicles Renew. Energies (EVER)*, Apr. 2016, pp. 1–9.

[13] C. Degen, "Inductive coupling for wireless power transfer and near-field communication," *EURASIP J. Wireless Commun. Netw.*, vol. 2021, no. 1, pp. 1–20, May 2021.

[14] V. T. Nguyen, S. H. Kang, J. H. Choi, and C. W. Jung, "Magnetic resonance wireless power transfer using three-coil system with single planar receiver for laptop applications," *IEEE Trans. Consum. Electron.*, vol. 61, no. 2, pp. 160–166, May 2015.

[15] J. Shin, S. Shin, Y. Kim, S. Ahn, S. Lee, G. Jung, S.-J. Jeon, and D.-H. Cho, "Design and implementation of shaped magnetic-resonance-based wireless power transfer system for roadway-powered moving electric vehicles," *IEEE Trans. Ind. Electron.*, vol. 61, no. 3, pp. 1179–1192, Mar. 2014.

[16] T. Shaw, S. Kayal, and D. Mitra, "Design of magnetic resonance coupled efficient wireless power transfer system using metamaterial," in *IEEE MTT-S Int. Microw. Symp. Dig.*, Dec. 2019, pp. 1–4.

[17] T. C. Beh, M. Kato, T. Imura, S. Oh, and Y. Hori, "Automated impedance matching system for robust wireless power transfer via magnetic resonance coupling," *IEEE Trans. Ind. Electron.*, vol. 60, no. 9, pp. 3689–3698, Sep. 2013.

[18] S. Maslovski, S. Tretyakov, and P. Alitalo, "Near-field enhancement and imaging in double planar polariton-resonant structures," *J. Appl. Phys.*, vol. 96, no. 3, pp. 1293–1300, Aug. 2004.

[19] A. A. Eteng, S. K. A. Rahim, C. Y. Leow, S. Jayaprakasam, and B. W. Chew, "Low-power near-field magnetic wireless energy transfer links: A review of architectures and design approaches," *Renew. Sustain. Energy Rev.*, vol. 77, pp. 486–505, Apr. 2017.

[20] R. E. Hamam, A. Karalis, J. D. Joannopoulos, and M. Soljačić, "Efficient weakly-radiative wireless energy transfer: An EIT-like approach," *Ann. Phys.*, vol. 324, no. 8, pp. 1783–1795, Aug. 2009.

[21] Y. Zhang, T. Lu, Z. Zhao, F. He, K. Chen, and L. Yuan, "Selective wireless power transfer to multiple loads using receivers of different resonant frequencies," *IEEE Trans. Power Electron.*, vol. 30, no. 11, pp. 6001–6005, Nov. 2015.

[22] K. Aydin and E. Ozbay, "Capacitor-loaded split ring resonators as tunable metamaterial components," *J. Appl. Phys.*, vol. 101, no. 2, Jan. 2007, Art. no. 024911.

[23] H. Hoang, S. Lee, Y. Kim, Y. Choi, and F. Bien, "An adaptive technique to improve wireless power transfer for consumer electronics," in *Proc. IEEE Int. Conf. Consum. Electron. (ICCE)*, Jan. 2012, pp. 359–360.

[24] J. Park, Y. Tak, Y. Kim, Y. Kim, and S. Nam, "Investigation of adaptive matching methods for near-field wireless power transfer," *IEEE Trans. Antennas Propag.*, vol. 59, no. 5, pp. 1769–1773, May 2011.

[25] M. E. Bima, I. Bhattacharya, W. O. Adepoju, and T. Banik, "Effect of coil parameters on layered DD coil for efficient wireless power transfer," *IEEE Lett. Electromagn. Compat. Pract. Appl.*, vol. 3, no. 2, pp. 56–60, Jun. 2021.

[26] S. Y. R. Hui, W. Zhong, and C. K. Lee, "A critical review of recent progress in mid-range wireless power transfer," *IEEE Trans. Power Electron.*, vol. 29, no. 9, pp. 4500–4511, Sep. 2014.

[27] C. J. Stevens, "Magnetoinductive waves and wireless power transfer," *IEEE Trans. Power Electron.*, vol. 30, no. 11, pp. 6182–6190, Nov. 2015.

[28] W. C. Cheah, S. A. Watson, and B. Lennox, "Limitations of wireless power transfer technologies for mobile robots," *Wireless Power Transf.*, vol. 6, no. 2, pp. 175–189, Sep. 2019.

[29] T. Ramachandran, M. R. I. Faruque, and M. T. Islam, "A dual band left-handed metamaterial-enabled design for satellite applications," *Results Phys.*, vol. 16, Mar. 2020, Art. no. 102942.

[30] M. J. Alam, M. R. I. Faruque, T. Allen, S. Abdullah, M. T. Islam, K. N. A. Maulud, and E. Ahamed, "Depiction and analysis of a modified theta shaped double negative metamaterial for satellite application," *Open Phys.*, vol. 16, no. 1, pp. 839–847, Dec. 2018.

[31] S. S. Islam, A. M. Tamim, and M. R. I. Faruque, "A new double-negative material for multi-band satellite applications," in *Proc. 10th Int. Conf. Robot., Vis., Signal Process. Power Appl.* Singapore: Springer, 2019, pp. 357–364.

[32] C. Liang, G. Young, J. J. Chen, and C. Chen, "A microcontroller-based implantable neuromuscular stimulation system with wireless power and data transmission for animal experiments," *J. Chin. Inst. Engineers*, vol. 26, no. 4, pp. 493–501, Jun. 2003.

[33] D. V. Nicolau, P. Livingston, D. Jahshan, and R. Evans, "An implantable remote-powered optoelectronic MEMS device for *in vivo* spectral analysis and biochemical tests," *Proc. SPIE*, vol. 5275, pp. 223–230, Mar. 2004.

[34] K. Goto, T. Nakagawa, O. Nakamura, and S. Kawata, "An implantable power supply with an optically rechargeable lithium battery," *IEEE Trans. Biomed. Eng.*, vol. 48, no. 7, pp. 830–833, Jul. 2001.

[35] K. Murakawa, M. Kobayashi, O. Nakamura, and S. Kawata, "A wireless near-infrared energy system for medical implants," *IEEE Eng. Med. Biol. Mag.*, vol. 18, no. 6, pp. 70–72, Nov./Dec. 1999.

[36] T. Campi, S. Cruciani, V. De Santis, and M. Feliziani, "EMF safety and thermal aspects in a pacemaker equipped with a wireless power transfer system working at low frequency," *IEEE Trans. Microw. Theory Techn.*, vol. 64, no. 2, pp. 375–382, Feb. 2016, doi: 10.1109/TMTT.2015.2514087.

[37] S. Cruciani, T. Campi, F. Maradei, and M. Feliziani, "Numerical simulation of wireless power transfer system to recharge the battery of an implanted cardiac pacemaker," in *Proc. Int. Symp. Electromagn. Compat.*, Sep. 2014, pp. 44–47.

[38] D. Newaskar and B. P. Patil, "Wireless charging of AIMDs-compensation circuits," in *Proc. Int. Conf. Comput. Perform. Eval. (ComPE)*, Jul. 2020, pp. 173–177.

[39] C. Xiao, D. Cheng, and K. Wei, "An LCC-C compensated wireless charging system for implantable cardiac pacemakers: Theory, experiment, and safety evaluation," *IEEE Trans. Power Electron.*, vol. 33, no. 6, pp. 4894–4905, Jun. 2018.

[40] Y. Jing, J. Xu, and N. X. Fang, "Numerical study of a near-zero-index acoustic metamaterial," *Phys. Lett. A*, vol. 376, no. 45, pp. 2834–2837, Oct. 2012.

[41] W.-C. Chen, C. M. Bingham, K. M. Mak, N. W. Caira, and W. J. Padilla, "Extremely subwavelength planar magnetic metamaterials," *Phys. Rev. B, Condens. Matter*, vol. 85, no. 20, May 2012, Art. no. 201104.

[42] E. S. G. Rodríguez, A. K. RamRakhyani, D. Schurig, and G. Lazzi, "Compact low-frequency metamaterial design for wireless power transfer efficiency enhancement," *IEEE Trans. Microw. Theory Techn.*, vol. 64, no. 5, pp. 1644–1654, May 2016.

[43] V. G. Veselago, "The electrodynamics of substances with simultaneously negative values of ε and μ," *Soviet Phys. Uspekhi*, vol. 10, no. 4, pp. 509–514, 1968, doi: 10.1070/PU1968v010n04ABEH003699.

[44] J. B. Pendry, "Negative refraction makes a perfect lens," *Phys. Rev. Lett.*, vol. 85, no. 18, pp. 3966–3969, Oct. 2000.

[45] E. Shamonina, V. A. Kalinin, K. H. Ringhofer, and L. Solymar, "Magneto-inductive waveguide," *Electron. Lett.*, vol. 38, no. 8, p. 371, 2002.

[46] E. Shamonina, V. A. Kalinin, K. H. Ringhofer, and L. Solymar, "Magnetoinductive waves in one, two, and three dimensions," *J. Appl. Phys.*, vol. 92, no. 10, pp. 6252–6261, Oct. 2002.

[47] C. J. Stevens, C. W. T. Chan, K. Stamatis, and D. J. Edwards, "Magnetic metamaterials as 1-D data transfer channels: An application for magneto-inductive waves," *IEEE Trans. Microw. Theory Techn.*, vol. 58, no. 5, pp. 1248–1256, May 2010.

[48] D. Ahn and S. Hong, "A study on magnetic field repeater in wireless power transfer," *IEEE Trans. Ind. Electron.*, vol. 60, no. 1, pp. 360–371, Jan. 2013.

[49] Z. Zhou, W. Li, Z. Deng, F. Li, Q. Shi, C. Cheng, and C. Mi, "An optimized multi-load wireless power transfer system with constant load currents," in *Proc. 10th Int. Conf. Power Electron. ECCE Asia (ICPE-ECCE Asia)*, May 2019, pp. 1–7.

[50] G. Puccetti, C. Stevens, U. Reggiani, and L. Sandrolini, "Experimental and numerical investigation of termination impedance effects in wireless power transfer via metamaterial," *Energies*, vol. 8, no. 3, pp. 1882–1895, Mar. 2015.

[51] Y. Urzhumov and D. R. Smith, "Metamaterial-enhanced coupling between magnetic dipoles for efficient wireless power transfer," *Phys. Rev. B, Condens. Matter*, vol. 83, no. 20, May 2011, Art. no. 205114.

[52] F. Bilotti, A. Toscano, L. Vegni, K. Aydin, K. B. Alici, and E. Ozbay, "Equivalent-circuit models for the design of metamaterials based on artificial magnetic inclusions," *IEEE Trans. Microw. Theory Techn.*, vol. 55, no. 12, pp. 2865–2873, Dec. 2007.

[53] C. Rong, C. Lu, Z. Hu, X. Huang, X. Tao, S. Wang, B. Wei, S. Wang, and M. Liu, "Analysis of wireless power transfer based on metamaterial using equivalent circuit," *J. Eng.*, vol. 2019, no. 16, pp. 2032–2035, Dec. 2018.

[54] J. D. Baena, J. Bonache, F. Martin, R. M. Sillero, F. Falcone, T. Lopetegi, M. A. G. Laso, J. Garcia-Garcia, I. Gil, M. F. Portillo, and M. Sorolla, "Equivalent-circuit models for split-ring resonators and complementary split-ring resonators coupled to planar transmission lines," *IEEE Trans. Microw. Theory Techn.*, vol. 53, no. 4, pp. 1451–1461, Apr. 2005.

[55] J.-F. Chen, Z. Ding, Z. Hu, S. Wang, Y. Cheng, M. Liu, B. Wei, and S. Wang, "Metamaterial-based high-efficiency wireless power transfer system at 13.56 MHz for low power applications," *Prog. Electromagn. Res.*, vol. 72, pp. 17–30, 2017.

[56] B. Wang, T. Nishino, and K. Hoo Teo, "Wireless power transmission efficiency enhancement with metamaterials," in *Proc. IEEE Int. Conf. Wireless Inf. Technol. Syst.*, Aug. 2010, pp. 1–4.

[57] B. Wang, K. H. Teo, T. Nishino, W. Yerazunis, J. Barnwell, and J. Zhang, "Experiments on wireless power transfer with metamaterials," *Appl. Phys. Lett.*, vol. 98, no. 25, Jun. 2011, Art. no. 254101.

[58] A. L. A. K. Ranaweera, T. P. Duong, and J.-W. Lee, "Experimental investigation of compact metamaterial for high efficiency mid-range wireless power transfer applications," *J. Appl. Phys.*, vol. 116, no. 4, Jul. 2014, Art. no. 043914.

[59] Y. Cho, J. J. Kim, D.-H. Kim, S. Lee, H. Kim, C. Song, S. Kong, H. Kim, C. Seo, S. Ahn, and J. Kim, "Thin PCB-type metamaterials for improved efficiency and reduced EMF leakage in wireless power transfer systems," *IEEE Trans. Microw. Theory Techn.*, vol. 64, no. 2, pp. 1–12, Feb. 2016.

[60] T. P. Duong and J.-W. Lee, "Experimental results of high-efficiency resonant coupling wireless power transfer using a variable coupling method," *IEEE Microw. Wireless Compon. Lett.*, vol. 21, no. 8, pp. 442–444, Aug. 2011.

[61] A. Rajagopalan, A. K. RamRakhyani, D. Schurig, and G. Lazzi, "Improving power transfer efficiency of a short-range telemetry system using compact metamaterials," *IEEE Trans. Microw. Theory Techn.*, vol. 62, no. 4, pp. 947–955, Apr. 2014.

[62] Y. Zhang, H. Tang, C. Yao, Y. Li, and S. Xiao, "Experiments on adjustable magnetic metamaterials applied in megahertz wireless power transmission," *AIP Adv.*, vol. 5, no. 1, Jan. 2015, Art. no. 017142.

[63] J. Chen and H. Tan, "Metamaterial for wireless power transfer system at 13.56 MHz with coil misalignment," in *Proc. 7th IEEE Int. Symp. Microw., Antenna, Propag., EMC Technol. (MAPE)*, Oct. 2017, pp. 313–317.

[64] A. Sihvola, "Metamaterials in electromagnetics," *Metamaterials*, vol. 1, no. 1, pp. 2–11, Mar. 2007.

[65] T. Shaw, A. Roy, and D. Mitra, "Efficiency enhancement of wireless power transfer system using MNZ metamaterials," *Prog. Electromagn. Res.*, vol. 68, pp. 11–19, 2016.

[66] R. Das, A. Basir, and H. Yoo, "A metamaterial-coupled wireless power transfer system based on cubic high-dielectric resonators," *IEEE Trans. Ind. Electron.*, vol. 66, no. 9, pp. 7397–7406, Sep. 2019.

[67] J. Zhang, J. Meng, W. Li, S. Yan, and A. E. Guy Vandenbosch, "A metamaterial inspired button antenna for wireless power and data transfer," in *Proc. IEEE 3rd Int. Conf. Electron. Inf. Commun. Technol. (ICEICT)*, Nov. 2020, pp. 341–343.

[68] F. Zhang, Q. Zhao, L. Kang, J. Zhou, and D. Lippens, "Experimental verification of isotropic and polarization properties of high permittivity-based metamaterial," *Phys. Rev. B, Condens. Matter*, vol. 80, no. 19, Nov. 2009, Art. no. 195119.

[69] C. L. Holloway, E. F. Kuester, J. Baker-Jarvis, and P. Kabos, "A double negative (DNG) composite medium composed of magnetodielectric spherical particles embedded in a matrix," *IEEE Trans. Antennas Propag.*, vol. 51, no. 10, pp. 2596–2603, Oct. 2003.

[70] L. Lewin, "The electrical constants of a material loaded with spherical particles," *J. Inst. Elect. Eng. III, Radio Commun. Eng.*, vol. 94, no. 27, pp. 65–68, Jan. 1947.

[71] S. O'Brien and J. B. Pendry, "Photonic band-gap effects and magnetic activity in dielectric composites," *J. Phys., Condens. Matter*, vol. 14, no. 15, p. 4035, 2002.

[72] Q. Zhao, J. Zhou, F. Zhang, and D. Lippens, "Mie resonance-based dielectric metamaterials," *Mater. Today*, vol. 12, no. 12, pp. 60–69, Dec. 2009.

[73] T. Shaw and D. Mitra, "Wireless power transfer system based on magnetic dipole coupling with high permittivity metamaterials," *IEEE Antennas Wireless Propag. Lett.*, vol. 18, no. 9, pp. 1823–1827, Sep. 2019.

[74] H. Wang, W. Wang, X. Chen, Q. Li, and Z. Zhang, "Analysis and design of kHz-metamaterial for wireless power transfer," *IEEE Trans. Magn.*, vol. 56, no. 8, pp. 1–5, Aug. 2020.

[75] D. R. Smith, S. Schultz, P. Markoš, and C. M. Soukoulis, "Determination of effective permittivity and permeability of metamaterials from reflection and transmission coefficients," *Phys. Rev. B, Condens. Matter*, vol. 65, no. 19, Apr. 2002, Art. no. 195104.

[76] S. S. Islam, M. A. Rahman, M. R. I. Faruque, and M. T. Islam, "Design and analysis with different substrate materials of a new metamaterial for satellite applications," *Sci. Eng. Compos. Mater.*, vol. 25, no. 1, pp. 59–66, Jan. 2018.

[77] N. Wang, X. Dong, W. Zhou, C. He, W. Jiang, and S. Hu, "Low-frequency metamaterial absorber with small-size unit cell based on corrugated surface," *AIP Adv.*, vol. 6, no. 2, Feb. 2016, Art. no. 025205.

[78] A. P. Sample, D. T. Meyer, and J. R. Smith, "Analysis, experimental results, and range adaptation of magnetically coupled resonators for wireless power transfer," *IEEE Trans. Ind. Electron.*, vol. 58, no. 2, pp. 544–554, Feb. 2011.

[79] V. T. Nguyen, S. H. Kang, and C. W. Jung, "Wireless power transfer for mobile devices with consideration of ground effect," in *Proc. IEEE Wireless Power Transf. Conf. (WPTC)*, May 2015, pp. 1–4.

[80] R. Tseng, B. von Novak, S. Shevde, and K. A. Grajski, "Introduction to the alliance for wireless power loosely-coupled wireless power transfer system specification version 1.0," in *Proc. IEEE Wireless Power Transf. (WPT)*, May 2013, pp. 79–83.

[81] D. Brizi, J. P. Stang, A. Monorchio, and G. Lazzi, "A compact magnetically dispersive surface for low-frequency wireless power transfer applications," *IEEE Trans. Antennas Propag.*, vol. 68, no. 3, pp. 1887–1895, Mar. 2020.

[82] C. Rong, C. Lu, and M. Liu, "Wireless power transfer system based on focused and shielding metamaterials," in *Proc. IEEE 4th Int. Electr. Energy Conf. (CIEEC)*, May 2021, pp. 1–4.

[83] C. Lu, X. Huang, X. Tao, C. Rong, and M. Liu, "Comprehensive analysis of side-placed metamaterials in wireless power transfer system," *IEEE Access*, vol. 8, pp. 152900–152908, 2020.

[84] Y. Cho, S. Lee, D.-H. Kim, H. Kim, C. Song, S. Kong, J. Park, C. Seo, and J. Kim, "Thin hybrid metamaterial slab with negative and zero permeability for high efficiency and low electromagnetic field in wireless power transfer systems," *IEEE Trans. Electromagn. Compat.*, vol. 60, no. 4, pp. 1001–1009, Aug. 2018.

[85] S. Lee, Y. Cho, S. Jeong, S. Hong, B. Sim, H. Kim, and J. Kim, "High efficiency wireless power transfer system using a two-stack hybrid metamaterial slab," in *Proc. IEEE Wireless Power Transf. Conf. (WPTC)*, Jun. 2019, pp. 616–619.

[86] T. P. Duong and J.-W. Lee, "A dynamically adaptable impedance-matching system for midrange wireless power transfer with misalignment," *Energies*, vol. 8, pp. 7593–7617, Aug. 2015.

[87] A. L. A. K. Ranaweera, C. A. Moscoso, and J.-W. Lee, "Anisotropic metamaterial for efficiency enhancement of mid-range wireless power transfer under coil misalignment," *J. Phys. D, Appl. Phys.*, vol. 48, no. 45, Oct. 2015, Art. no. 455104.

[88] S. Wang, C. Jiang, X. Tao, F. Chen, C. Rong, C. Lu, Y. Zeng, X. Liu, R. Liu, B. Wei, and M. Liu, "Enhancing the stability of medium range and misalignment wireless power transfer system by negative magnetic metamaterials," *Materials*, vol. 13, no. 24, p. 5695, Dec. 2020.

[89] E. Jabari and E. Toyserkani, "Aerosol-Jet printing of highly flexible and conductive graphene/silver patterns," *Mater. Lett.*, vol. 174, pp. 40–43, Jul. 2016.

[90] Chemcubedllc. (2018). *Multi-Layer/Multi-Material Digital Printing Solutions for Electronics*. Accessed: Jun. 26, 2019. [Online]. Available: https://www.chemcubed.com/electrojet

[91] N. Dimension. *Precision Additive Manufacturing of Printed Electronics*. Accessed: Jun. 6, 2019. [Online]. Available: https://www.nano-di.com/dragonfly-pro-3d-printer

[92] P. S. Karthik and S. P. Singh, "Conductive silver inks and their applications in printed and flexible electronics," *RSC Adv.*, vol. 5, no. 95, pp. 77760–77790, 2015.

[93] Voxel8. (2016). *Silver Conductive Ink Technical Data Sheet.* Accessed: Jun. 29, 2019. [Online]. Available: https://p4.zdassets

[94] J. J. Adams, B. E. Duoss, F. T. Malkowski, J. M. Motala, B. YeopAhn, G. R. Nuzzo, T. J. Bernhard, and A. J. Lewis, "Conformal printing of electrically small antennas on three-dimensional surfaces," *Adv. Mater.*, vol. 23, no. 11, pp. 1335–1340, Mar. 2011.

[95] F. Wang, P. Mao, and H. He, "Dispensing of high concentration ag nanoparticles ink for ultra-low resistivity paper-based writing electronics," *Sci. Rep.*, vol. 6, no. 1, pp. 1–8, Feb. 2016.

[96] E. Balliu, H. Andersson, M. Engholm, T. Öhlund, H.-E. Nilsson, and H. Olin, "Selective laser sintering of inkjet-printed silver nanoparticle inks on paper substrates to achieve highly conductive patterns," *Sci. Rep.*, vol. 8, no. 1, pp. 1–9, Jul. 2018.

[97] F. Bilotti, A. Toscano, and L. Vegni, "Design of spiral and multiple splitring resonators for the realization of miniaturized metamaterial samples," *IEEE Trans. Antennas Propag.*, vol. 55, no. 8, pp. 2258–2267, Aug. 2007.

[98] J. D. Baena, R. Marqués, F. Medina, and J. Martel, "Artificial magnetic metamaterial design by using spiral resonators," *Phys. Rev. B, Condens. Matter*, vol. 69, no. 1, Jan. 2004, Art. no. 014402.

[99] K. Buell, H. Mosallaei, and K. Sarabandi, "A substrate for small patch antennas providing tunable miniaturization factors," *IEEE Trans. Microw. Theory Techn.*, vol. 54, no. 1, pp. 135–146, Jan. 2006.

[100] C. Hoer and C. Love, "Exact inductance equations for rectangular conductors with applications to more complicated geometries," *J. Res. Nat. Bur. Standards, C, Eng. Instrum.*, vol. 69, no. 2, p. 127, Apr. 1965.

[101] Z. Luo and X. Wei, "Analysis of square and circular planar spiral coils in wireless power transfer system for electric vehicles," *IEEE Trans. Ind. Electron.*, vol. 65, no. 1, pp. 331–341, Jan. 2018.

WEBSTER ADEPOJU (Student Member, IEEE) received the Bachelor of Science degree in electrical and electronic engineering from Obafemi Awolowo University, Nigeria, and the Master of Engineering degree (Hons.) in electrical and electronic engineering from the University of Johannesburg (UJ), South Africa. He is currently pursuing the Ph.D. degree in electrical and computer engineering with the SOLBAT-TTU Energy Research Laboratory, Tennessee Technological University, USA. From 2018 to 2019, he was a Research Assistant with the Centre for Telecommunication, UJ, where he investigated the effect of common mode and differential mode noise on cables used for power line communication. Prior to this, he worked on the modeling and control of high-gain DC–DC converters, observer-based sensor-less systems, and advanced model predictive control of single phase inverter. His current research interests include low frequency metamaterial-based wireless power transfer, power electronics, wide band gap devices, and semiconductor modeling. He was a recipient of the 2021 Best Poster Presentation Award at the University's Research and Creative Inquiry Day.

INDRANIL BHATTACHARYA (Member, IEEE) received the Bachelor of Engineering degree (Hons.) in electronics and communication engineering from India and the M.S. and Ph.D. degrees in electrical engineering from Florida State University. He is currently an Associate Professor (tenured) with the Electrical and Computer Engineering Department, Tennessee Technological University. He is the main inventor of two U.S. patents. He has been the Principal or a Co-Principal Investigator of USD 2.5 million funding from agencies, like the National Science Foundation, the U.S. Department of Energy, and the Oak Ridge National Laboratory. He has published 43 peer-reviewed technical papers in reputed journals and conferences. He has supervised seven Ph.D., 11 master's, and 50 undergraduate students. His research interests include lithium and sodium-based battery technologies, high-efficiency III–V solar cells, wireless power transfer, and electromagnetics.

MARY SANYAOLU received the bachelor's degree from the University of Lagos and the master's degree from the University of Johannesburg, South Africa. From 2014 to 2015, she was an Intern with Oando Oil Corporation. She was with the University of Johannesburg, from 2017 to 2021. She is currently a Geo-Technical Consultant at GasFleet Engineering. Her current research interests include nano-materials and material characterization, modeling, and analysis. She was a recipient of the prestigious Global Excellence Scholarship and the National Research Fellowship.

MUHAMMAD ENAGI BIMA (Student Member, IEEE) received the Bachelor of Engineering degree in electrical and computer engineering from the Federal University of Technology Minna, the master's degree in communication engineering from The University of Manchester, and the Ph.D. degree in engineering from Tennessee Technological University, with a focus on wireless power transfer. During this period, he worked as a Research Assistant at the SOLBAT-TTU Energy Research Laboratory. He also interned at ANSYS Inc., at the Research and Development Quality Assurance Unit. He taught at the Mechatronics Engineering Department, Federal University of Technology Minna, where he mentored and taught students. He is currently a Software Engineer at Nordstrom Inc. He was a recipient of the College of Engineering Eminence Award for the Doctor of Philosophy Best Paper, in 2020. He was also awarded the Best Poster Presentation Award at the 2020 and 2021 Research and Creative Inquiry Days at the University.

TRAPA BANIK received the B.S. degree from the Chittagong University of Engineering and Technology, Bangladesh. She is currently pursuing a Ph.D. degree in electrical and computer engineering with Tennessee Technological University, under the supervision of Dr. Indranil Bhattacharya. Her research interests include sodium ion battery, wireless power transfer, electric vehicle systems, renewable energy, and smart grid systems.

EBRAHIM N. ESFAHANI received the B.S. degree in electrical engineering from Kashan University, Iran, in 2007, and the M.S. degree in electrical engineering from IAUN, Iran, in 2010. He is currently pursuing the Ph.D. degree in electrical and computer engineering with Tennessee Technological University, Cookeville, TN, USA. He was in the industry as an Electrical Maintenance Engineer at the steel company for more than eight years. His research interests include design and analysis of electric machines, modeling of electromagnetic devices, and wireless power transfer.

OLATUNJI ABIODUN received the B.Sc. degree (Hons.) in electrical and electronics engineering from Great Obafemi Awolowo University, Nigeria. He is currently pursuing the master's degree with the Electrical and Computer Engineering Department, Tennessee Technological University. He has six years industrial experience in electrical and electronics engineering related fields. His research interests include wireless power transfer, high frequency transformers, and electric vehicles.

● ● ●